ADVANCED ENERGY MATERIALS
www.advenergymat.de

Molecular Engineering of Layered Halide Double Perovskites: Challenges and Opportunities in Optoelectronics and Beyond

Maryam Ghasemi, Pelin Karsili, Anamika Mishra, Mohammad Reza Golobostanfard, and Jovana V. Milić**

Metal halide perovskites have become the leading semiconductors for new-generation optoelectronics. However, they are primarily based on toxic lead components, which pose environmental concerns. To address this critical limitation, there is an effort to design alternative lead-free halide perovskite materials. One of the emerging approaches has involved the use of layered (2D) halide double perovskite (LDP) materials incorporating tailored organic spacers within the lead-free perovskite framework based on alternative monovalent (M^{I}) and trivalent (M^{III}) metal cations, such as Ag, Bi, Cu, In, and others. The interactions within the assemblies of these hybrid organic–inorganic structures define the resulting properties. The role of molecular engineering in the development of LDPs and their optoelectronic characteristics is reviewed from the perspective of molecular design, synthesis, and functionality. Their versatility and methods to synthesize LDPs are discussed, as well as emerging applications, revealing challenges, and opportunities for their utility in more sustainable perovskite optoelectronics and beyond.

1. Introduction

Metal halide perovskite semiconductors have been transformative in optoelectronics, including photovoltaics, light-emitting diodes (LEDs), photodetectors, lasers, and ferroelectrics.[1,2] These materials are based on AMX_3 compositions, defining the corner-sharing $\{MX_6\}$ octahedral framework (**Figure 1**) incorporating divalent metal cations (M, typically Pb^{2+}) and halide anions (X = I, Br, Cl), while hosting central A cations, which can be either inorganic (e.g., Cs^+) or small organic moieties (e.g., methylammonium (MA)). They exhibit exceptional optoelectronic characteristics, resulting in remarkable solar-to-electric power conversion efficiencies, although conventionally prepared through the solution-processing of thin films.[3,4] Despite these advantages, metal halide perovskites face critical limitations that hamper their practical application.[4–6] In particular, they are unstable against external environmental factors, such as oxygen and moisture, as well as under device operating conditions of bias and light that accelerate ionic migration, detrimental to the stability and performance.[7–9] Moreover, they are mostly based on toxic Pb components, which are harmful to the environment and require more sustainable alternatives.[10–16] To address these challenges, there has been an effort to design alternative yet operationally stable and effective lead-free perovskite materials.[11,13]

One of the most prominent approaches involves the use of layered (2D) perovskites based on the incorporation of organic (spacer) cations within the inorganic perovskite framework (Figure 1, middle),[17] enhancing the stability due to their hydrophobicity and ion impermeability.[18–21] These materials are typically represented by the $S_xA_{n-1}M_nX_{3n+1}$ formulae, describing a layered structure defined by the organic spacers (S) templating the octahedral framework. The spacers are commonly mono- ($x = 2$) or bifunctional ($x = 1$) ammonium cations, forming mostly Ruddlesden–Popper (RP) and Dion–Jacobson (DJ) 2D phases, respectively (**Figure 2**).[18,19,21] The interactions between the components within the hybrid 2D assemblies define their properties,[20–23] and (supra)molecular engineering can be used in this context.[3,24–26] To develop lead-free alternatives, the use of halide double perovskites based on more environmentally friendly monovalent (M^{I}) and trivalent (M^{III}) cations is relevant including Ag^+, Cu^+, In^{3+}, and Bi^{3+} that replace toxic Pb^{2+} in $A_2M^{I}M^{III}X_6$ compositions (X = I, Br, Cl; Figure 1).[10,27,28] These systems offer advantages and versatility, preserving perovskite-like properties while increasing their stability. However, their application in optoelectronic devices is still underexplored.[29–34] In particular, among various possible double perovskite materials,[10,28] only Ag^+, Bi^{3+}/In^{3+}-containing systems have so far demonstrated solution-processability under moderate temperatures (<150 °C) that can be applied to thin

M. Ghasemi, P. Karsili, A. Mishra, M. R. Golobostanfard, J. V. Milić
Department of Chemistry
University of Turku
Turku 20500, Finland
E-mail: mohammadreza.golobostanfard@utu.fi; jovana.milic@utu.fi

The ORCID identification number(s) for the author(s) of this article can be found under https://doi.org/10.1002/aenm.202502693

DOI: 10.1002/aenm.202502693

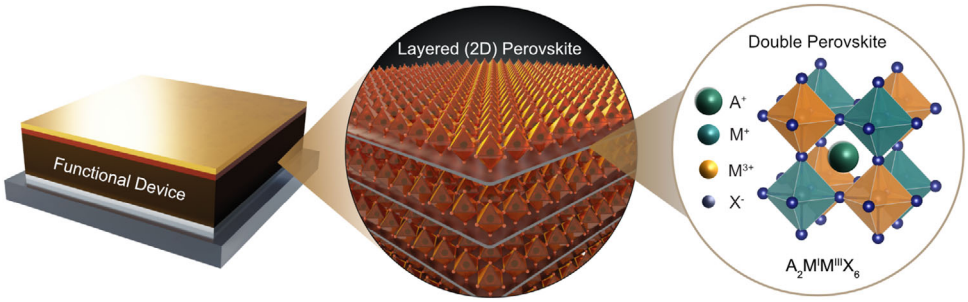

Figure 1. Schematic of the LDP devices. LDP structure containing double perovskite 3D $AM^{I}M^{III}X_6$ perovskite layers templated by organic spacers within a functional perovskite device. Adapted with permission from ref. [38]. Copyright 2024, John Wiley and Sons.

films and functional devices,[10,28,30,32,34] whereas $Cs_2M^{I}M^{III}X_6$ compositions were used in solar cells.[10,31,32,34–36] While 3D $A_2M^{I}M^{III}X_6$ double perovskites offer improved stability in lead-free compositions, their optoelectronic properties are often sub-optimal due to indirect bandgaps and limited carrier mobility. It is thus critical to identify stable lead-free alternatives with desirable optoelectronic properties.[10,37]

Layered double perovskites (LDPs) incorporating organic spacers in RP or DJ phases (Figure 2) were first reported in 2017,[22,29,39–42] offering a new platform for more stable lead-free halide perovskites. Although LDPs often deviate from the ideal AMX_3 3D structure, the terminology "perovskite" remains widely used based on their structural origin and functional equivalence to traditional perovskites.[43] They feature corner-sharing octahedral subnetworks and exhibit attractive optoelectronic properties, which have recently garnered widespread attention due to their stability, tunability, and inherent modularity in composition and design.[42] Despite their exciting potential, research on LDPs is still in its early stages, and their structure–property relationships, as well as mechanisms of operation, remain to be explored.

Here, we review the emerging class of halide LDP materials from the perspective of their molecular engineering and the impact of the molecular components on the resulting structural and optoelectronic characteristics relevant to their functional device applications. We further discuss challenges and opportunities for advancing their properties for optoelectronics and beyond.

2. Molecular Engineering of LDPs

LDP materials are templated by the organic spacer cations incorporated within the inorganic perovskite framework, with a critical role in determining their structure and optoelectronic properties.[18,19,21] This primarily involves alkyl and aryl ammonium spacer cations due to geometric compatibility and electrostatic interactions with the octahedral framework by hydrogen bonding (**Table 1**).[20–23] Similar to the other 2D halide perovskites, LDPs are mostly represented by $(S)_{2x}A_{2(n-1)}(M^{I}M^{III})_nX_{2(3n+1)}$ compositions (n = 1, 2, 3, etc.). While monofunctional spacer cations (S) primarily form the RP phases through an organic spacer bilayer (x = 2) and displacement between the adjacent inorganic slabs, the bifunctional moieties (x = 1) commonly yield well-aligned DJ perovskite phases (Figure 2, top). Their composition and intermolecular interactions determine the structure and optoelectronic properties.[3,24–26] Most of the double perovskites to date are based on Br^- or Cl^- counter ions due to the large ionic radius of I^-. To form a stable structure, the octahedral ratio, $\mu = r(M^{3+})/r(X^-)$, should typically be ≥0.41, where $r(M^{3+})$ and $r(X^-)$ are the radii of the metal cation and halide, anion respectively.[22,29,39–42] Only a few M^{3+} cations can meet this requirement with the large I^- radius. For instance, Ag^+ is significantly less likely to form regular octahedral coordination with I^- ions due to its higher distortion index than that of Bi^{3+}, further limiting the formation of I-based double perovskites, such as Cs_2AgBiI_6. However, they have been stabilized by LDPs, which allow for a diverse selection of cations with possible stabilizing effects.[41] Molecular design of organic spacers and their interactions thus offers structural modularity, of LDPs enabling control over crystal symmetry, dimensionality, and dielectric behavior defining their application.

Early efforts toward molecular engineering of LDPs were stimulated by their ferroelectricity.[44] Ferroelectric materials exhibit spontaneous polarization reversed by an external electric field, making them attractive for memory storage, sensors, actuators, and photovoltaics. Paraelectric–ferroelectric phase transitions from noncentrosymmetric to centrosymmetric space groups are directly associated with the emergence of spontaneous polarization (Ps) in ferroelectrics.[44] In LDPs, the orientation, symmetry, and dynamic behavior of organic cations influence the emergence of noncentrosymmetric phases, and understanding of the underlying structure–property relationships is key to enabling their functionality and future applications.[45] The main molecular strategies for enabling ferroelectricity and application in optoelectronics include the use of cyclic and polar organic cations, halogen substitution, and chiral moieties, which promote noncentrosymmetric phases relevant to the ferroelectric behavior.[46] Here, molecular engineering enabled accessing phase transitions, typically involving a change from a noncentrosymmetric to a centrosymmetric space group, with Ps and higher Curie temperatures (Tc) that are better suited for practical applications.[47,48] Moreover, the organic spacer cations and their interactions influence the octahedral connectivity and, consequently, govern other functionalities.

The first examples of LDP ferroelectrics relied on the use of alkylammonium cations, as temperature-dependent phase transitions can be triggered by the reorientation and rotation of the alkyl chain.[49,50] Such conformational changes in the organic spacer layers are translated into phase transitions of the layered perovskite systems. This effect was particularly apparent in the RP phases based on short propylammonium (PA) cations, as in $(PA)_4AgBiBr_8$ compositions.[29,51,52]

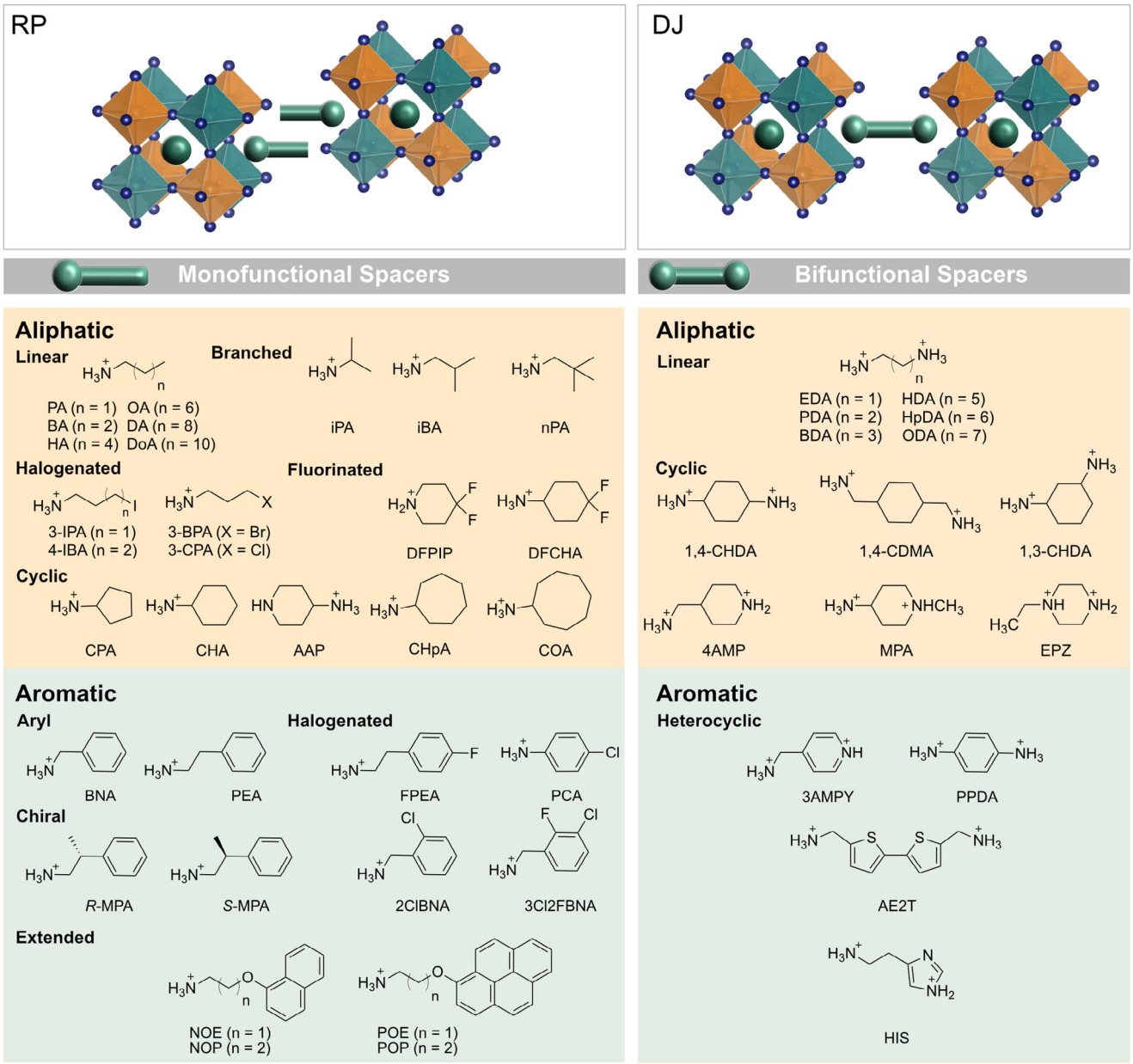

Figure 2. Structural representation of LDPs and the corresponding organic spacer cations. RP (left) and DJ (right) LDP phases with the corresponding mono- and bifunctional spacer cations (below). AAP = 4-aminopiperidinium; AE2T = 5,5′-diylbis(aminoethyl)-[2,2′-bithiophene]; 3AMPY = 3-(aminomethyl)pyridinium; 4AMP = 4-(ammoniummethyl)piperidinium; BA = *n*-butylammonium; BDA = 1,4-butanediammonium; BNA = benzylammonium; 3-BPA = 3-bromopropylammonium; 2ClBNA = 2-chlorobenzylammonium; 3Cl2FBNA = 3-chloro-2-fluorobenzylammonium; 1,3-CHDA = 1,3-diammoniumcyclohexane; 1,4-CHDA = 1,4-cyclohexyldiammonium; 1,4-CDMA = 1,4-bis(methylammonium)cyclohexane; CHA = cyclohexylammonium; CHpA = cycloheptylammonium; COA = cyclooctylammonium; CPA = cyclopentylammonium; 3-CPA = 3-chloropropylammonium; DA = decylammonium; DFCHA = 4,4-difluorocyclohexylammonium; DFPIP = 4,4-difluoropiperidinium; DoA = dodecylammonium; EDA = ethylenediammonium; FPEA = 4-fluorophenethylammonium; HA = hexylammonium; HIS = histammonium; MPA = 1-methylpiperidinium-4-ammonium; EPZ = 1-ethylpiperazinium; HDA = hexane-1,6-diammonium; HpDA = heptane-1,7-diammonium; iBA = isobutylammonium; 4-IBA = 4-iodobutylammonium; iPA = isopropylammonium; 3-IPA = 3-iodopropylammonium; S/R-MPA = *S/R*-(+/−)-*β*-methylphenethylammonium; nPA = neopentylammonium; NOE = naphthalene-*O*-ethylammonium; NOP = naphthalene-*O*-propylammonium; ODA = octane-1,8-diammonium; OA = n-octylammonium; PA = *n*-propylammonium; PCA = *p*-chloroanilinium; PDA = propane-1,3-diammonium; PEA = 2-phenylethylammonium; POE = pyrene-*O*-ethylammonium; POP = pyrene-*O*-propylammonium; PPDA = *p*-phenylenediammonium. The corresponding spacer cations and reports are summarized in Table 1.

Table 1. Summary of the reports on spacer cations and their LDPs composition and phases.

Nos.	Organic spacer	LDP composition	Phase [*n*]	Refs.
Monofunctional spacer cations				
1	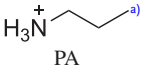 PA	$(PA)_4AgInCl_8$	RP ($n = 1$)	[29]
		$(PA)_4AgBiBr_8$	RP ($n = 1$)	[29]
		$(PA)_4AgInBr_8$	RP ($n = 1$)	[29]
		$(PA)_2CsAgBiBr_7$	RP ($n = 2$)	[29]
		$(PA)_2CsAgIn_{0.5}Bi_{0.5}Br_7$	RP ($n = 2$)	[29]
		$(PA)_2CsAgInBr_7$	RP ($n = 2$)	[29]
		$(PA)_2CsAgBiBr_7$	RP ($n = 2$)	[51]
		$(PA)_4CuInCl_8$	RP ($n = 1$)	[52]
		$Cl_{1.14}Br_{2.86}(PA_4)AgInBr_8$	RP ($n = 1$)	[48]
2	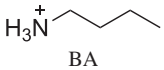 BA	$(BA)_4AgBiBr_8$	RP ($n = 1$)	[39]
		$(BA)_2CsAgBiBr_7$	RP ($n = 2$)	[39]
		$(BA)_4AgBiBr_8$	RP ($n = 1$)	[92]
		$(BA)_4AgBiBr_8$	RP ($n = 1$)	[55]
		$(BA)_2CsAgBiBr_7$	RP ($n = 2$)	[54]
		$(BA)_2CsAgTlBr_7$	RP ($n = 2$)	[39]
		$(BA)_2CsAgBiBr_7$	RP ($n = 2$)	[93]
		$(BA)_2CsAgBiBr_7/Cs_2AgBiBr_6$	RP ($n = 2$)	[56]
3	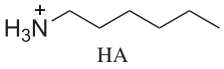 HA	$(HA)_4AgBiBr_8$	RP ($n = 1$)	[57]
4	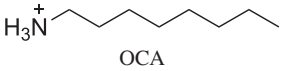 OCA	$(OCA)_4AgBiBr_8$	RP ($n = 1$)	[29]
5	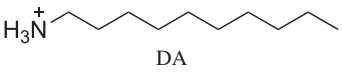 DA	$(DA)_4AgBiBr_8$	RP ($n = 1$)	[29]
		$(DA)_2CsAgBiBr_7$	RP ($n = 2$)	[94]
6	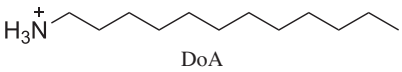 DoA	$(DoA)_4AgBiBr_8$	RP ($n = 1$)	[94]
		$(DoA)_2CsAgBiBr_7$	RP ($n = 2$)	[94]
7	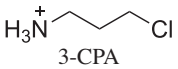 3-CPA	$Cl_{0.97}Br_{3.03}$ (3-CPA)$_4AgBiBr_8$	RP ($n = 1$)	[47]
		(3-CPA)$_4AgBiBr_8$	RP ($n = 1$)	[82]
8	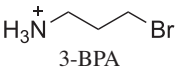 3-BPA	(3-BPA)$_4AgTlBr_8$	RP ($n = 1$)	[39]
		(3-BPA)$_4AgInBr_8$	RP ($n = 1$)	[39]
		(3-BPA)$_4AgBiI_8$	RP ($n = 1$)	[90]
		(3-BPA)$_4AgBiBr_8$	RP ($n = 1$)	[47]
9	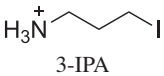 3-IPA	(3-IPA)$_4AgBiI_8$	RP (n = 1)	[95]
10	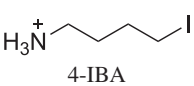 4-IBA	(4-IBA)$_4AgBiI_8$	RP ($n = 1$)	[83]
11	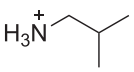 iBA	(iBA)$_4AgBiBr_8$	RP ($n = 1$)	[57]
		(iBA)$_2CsAgBiBr_7$	RP ($n = 2$)	[65]
12	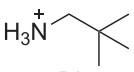 nPA	(nPA)$_4AgBiBr_8$	RP ($n = 1$)	[49]

(*Continued*)

Table 1. (Continued)

Nos.	Organic spacer	LDP composition	Phase [*n*]	Refs.
13	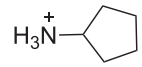 CPA	$(CPA)_4AgBiI_8$	RP ($n = 1$)	[96]
		$(CPA)_4AgSbI_8$	RP ($n = 1$)	[86]
14	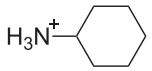 CHA	$(CHA)_4AgBiI_8$	RP ($n = 1$)	[96]
		$(CHA)_4CuSbI_8{\cdot}H_2O$	RP ($n = 1$)	[97]
		$(CHA)_4AgSbBr_8$	RP ($n = 1$)	[77]
		$(CHA)_4CuBiI_8$	RP ($n = 1$)	[67]
		$(CHA)_4AgSbI_8$	RP ($n = 1$)	[86]
15	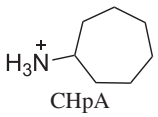 CHpA	$(CHpA)_4CuBiI_8$	RP ($n = 1$)	[67]
16	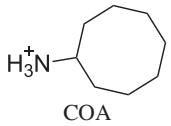 COA	$(COA)_4AgSbI_8$	RP ($n = 1$)	[86]
		$(COA)_4CuBiI_8$	RP ($n = 1$)	[67]
17	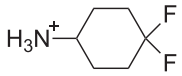 DFCHA	$(DFCHA)_4AgSbBr_8$	RP ($n = 1$)	[77]
18	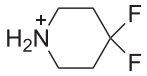 DFPIP	$(DFPIP)_4AgBiI_8$	RP ($n = 1$)	[80]
		$(DFPIP)_4AgSbI_8$	RP ($n = 1$)	[81]
		$(DFPIP)_4AgSbBr_8$	RP ($n = 1$)	[77]
19	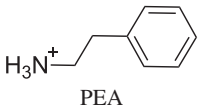 PEA	$(PEA)_4BiAgBr_8$	RP ($n = 1$)	[74]
		$(PEA)_4BiAgI_8$	RP ($n = 1$)	[74]
		$(PEA)_2CsAgTlBr_7$	RP ($n = 2$)	[39]
		$(PEA)_4CuInCl_8$	RP ($n = 1$)	[98, 99]
		$(PEA)_4NaInCl_8$	RP ($n = 1$)	[100]
		$(PEA)_4AgFeCl_8$	RP ($n = 1$)	[60]
		$(PEA)_4NaIn_{(1-x)}Fe_xCl_8$ ($0 \le x \le 1$)	RP ($n = 1$)	[101]
		$(PEA)_4NaFeCl_8$	RP ($n = 1$)	[60]
		$(PEA)_4NaInCl_8$	RP ($n = 1$)	[88]
		$(PEA)_2CsNaInCl_7$	RP ($n = 2$)	[88]
		$(PEA)_4AgBiBr_8$	RP ($n = 1$)	[102]
		$(PEA)_4AgInCl_8$	RP ($n = 1$)	[102]
20	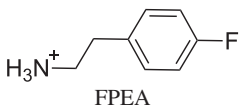 FPEA	$(FPEA)_4AgBiBr_8$	RP ($n = 1$)	[76]
21	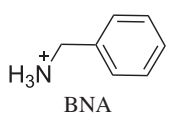 BNA	$(BNA)_2CsAgBiBr_7$	RP ($n = 2$)	[69]
		$(BNA)_4AgBiBr_8$	RP ($n = 1$)	[102]
		$(BNA)_4AgInCl_8$	RP ($n = 1$)	[102]

(*Continued*)

Table 1. (Continued)

Nos.	Organic spacer	LDP composition	Phase [*n*]	Refs.
22	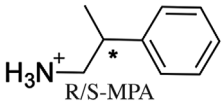 R/S-MPA	$(R\text{-}MPA)_4AgBiI_8$	RP ($n = 1$)	[91]
		$(S\text{-}MPA)_4AgBiI_8$	RP ($n = 1$)	[91]
		$(R\text{-}MPA)_4AgFeCl_8$	RP ($n = 1$)	[60]
23	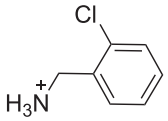 2ClBNA	$(2ClBNA)_4AgBiBr_8$	RP ($n = 1$)	[84]
24	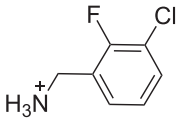 3Cl2FBNA	$(3Cl2FBNA)_4AgBiBr_8$	RP ($n = 1$)	[84]
25	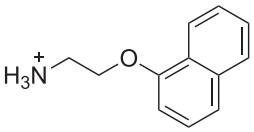 NOE	$(NOE)_4AgBiI_8$	RP ($n = 1$)	[89]
		$(NOE)_4CuBiI_8$	RP ($n = 1$)	[89]
26	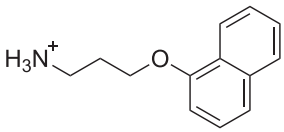 NOP	$(NOP)_4AgBiI_8$	RP ($n = 1$)	[89]
		$(NOP)_4CuBiI_8$	RP ($n = 1$)	[89]
27	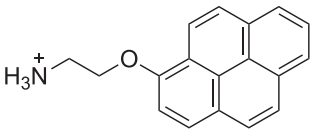 POE	$(POE)_4AgBiI_8$	RP ($n = 1$)	[89]
		$(POE)_4CuBiI_8$	RP ($n = 1$)	[89]
28	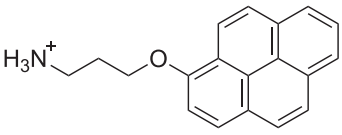 POP	$(POP)_4AgBiI_8$	RP ($n = 1$)	[89]
		$(POP)_4CuBiI_8$	RP ($n = 1$)	[89]
Bifunctional spacer cations				
29	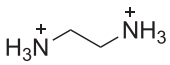 EDA	$(EDABr)_4AgBiBr_8$	DJ ($n = 1$)	[62]
		$(EDABr)_4CuBiBr_8$	DJ ($n = 1$)	[62]
		$(EDABr)_4AgBiBr_8$	DJ ($n = 1$)	[61]
30	 PDA	$(PDA)_2AgRuCl_8$	DJ ($n = 1$)	[53]
		$(PDA)_2AgRuBr_8$	DJ ($n = 1$)	[53]
		$(PDA)_2AgBiBr_8$	DJ ($n = 1$)	[61]
31	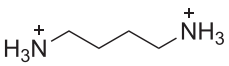 BDA	$(BDA)_2CuInCl_8$	DJ ($n = 1$)	[52]
		$(BDA)_2CuRuCl_8$	DJ ($n = 1$)	[52]
		$(BDA)_2AgBiBr_8$	DJ ($n = 1$)	[58]
		$(BDA)_2AgSbBr_8$	DJ ($n = 1$)	[58]
		$(BDA)_2AgBiBr_8$	DJ ($n = 1$)	[103]

(*Continued*)

Table 1. (Continued)

Nos.	Organic spacer	LDP composition	Phase [*n*]	Refs.
		$(BDA)_2AgBiBr_8$	DJ ($n = 1$)	[29]
		$(BDA)_2AgRuBr_8$	DJ ($n = 1$)	[53]
		$(BDA)_2AgRuCl_8$	DJ ($n = 1$)	[53]
		$(BDA)_2AgRuBr_8$	DJ ($n = 1$)	[53]
		$(BDA)_2CuBiI_8$	DJ ($n = 1$)	[64]
		$(BDA)_2AgFeCl_8$	DJ ($n = 1$)	[60]
		$(BDA)_4AgBiBr_8$	DJ ($n = 1$)	[61]
32	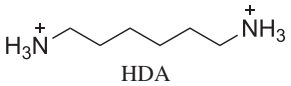 HDA	$(HDA)_2AgBiBr_8$	DJ ($n = 1$)	[58]
33	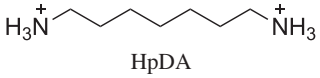 HpDA	$(HpDA)_2Au^{I}Au^{III}I_6.I_3$	DJ ($n = 1$)	[59]
34	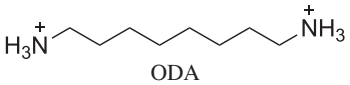 ODA	$(ODA)_2Au^{I}Au^{III}I_6.I_3$	DJ ($n = 1$)	[59]
35	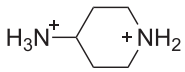 AAP	$(AAP)_4[Bi.Ag.I_8].H_2O$	1D	[85]
36	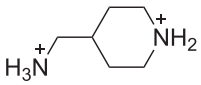 4AMP	$(4AMP)_2AgBiI_8.0.5H_2O$	1D	[104]
		$(4AMP)_4[Bi.Ag.I_8]_2.H_2O$	1D	[85]
37	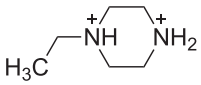 EPZ	$(EPZ)_2BiAgBr_8$	DJ ($n = 1$)	[105]
38	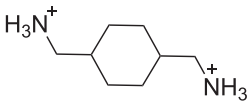 1,4-CDMA	$(1,4\text{-}CDMA)_2AgInBr_8$	DJ ($n = 1$)	[68]
		$(1,4\text{-}CDMA)_2AgSbBr_8$	DJ ($n = 1$)	[68]
		$(1,4\text{-}CDMA)_2AgBiBr_8$	DJ ($n = 1$)	[68]
39	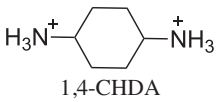 1,4-CHDA	$(1,4\text{-}CHDA)_2AgSbI_8.H_2O$	1D	[86]
		$(1,4\text{-}CHDA)_2AgSbI_8$	DJ ($n = 1$)	[86]
		$(1,4\text{-}CHDA)_2AgBiI_8.H_2O$	1D	[66]
		$(1,4\text{-}CHDA)_2CuBiI_8.0.5H_2O$	1D	[66]
		$(1,4\text{-}CHDA)_2CuSbI_8{\cdot}0.5H_2O$	1D	[97]
40	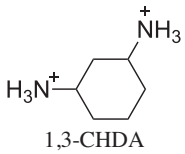 1,3-CHDA	$(1,3\text{-}CHDA)_2CuBiI_8$	DJ ($n = 1$)	[67]
41	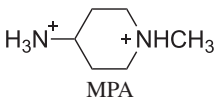 MPA	$(MPA)_2BiAgBr_8$	DJ ($n = 1$)	[105]
		$(MPA)_2CuBiI_8$	DJ ($n = 1$)	[67]

(*Continued*)

Table 1. (Continued)

Nos.	Organic spacer	LDP composition	Phase [*n*]	Refs.
42	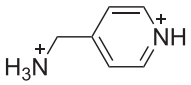 3AMPY	$(3AMPY)_2AgBiI_8.H_2O$	DJ ($n = 1$)	[104]
		$(4AMP)_2AgBiBr_8$	DJ ($n = 1$)	[50]
43	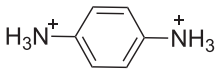 PPDA	$(PPDA)_2AgRuCl_8$	DJ ($n = 1$)	[53]
		$(PPDA)_2CuRuCl_8$	DJ ($n = 1$)	[53]
		$(PPDA)_2AgMoCl_8$	DJ ($n = 1$)	[53]
44	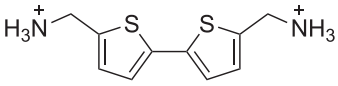 AE2T	$(AE2T)_2AgBiI_8$	DJ ($n = 1$)	[41]
45	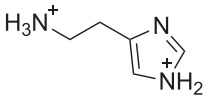 HIS	$(CuCl_2)_4(HIS)_4CuInCl_8$	DJ ($n = 1$)	[98]
		$(HIS)_2AgBiBr_8$	DJ ($n = 1$)	[106]
Selected systematic comparisons with monofunctional cations				
46	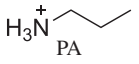 PA 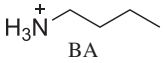 BA 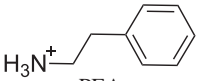 PEA	$(S)_4AgBiBr_8$ S = PA, BA, PEA, DA, DoA	RP ($n = 1$)	[94]
	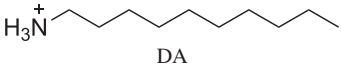 DA 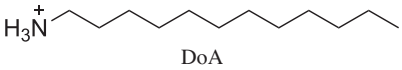 DoA	$(S)_2CsAgBiBr_7$ S = BA, PEA, DA, DoA	RP ($n = 2$)	[94]
47	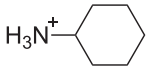 CHA 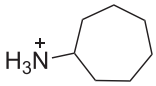 CHpA 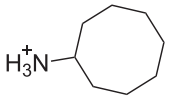 COA	$(S)_4CuBiI_8$ S = CHA, CHpA, COA	RP ($n = 1$)	[67]
48	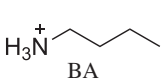 BA 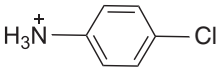 PCA 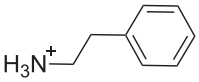 PEA	$(S)_4[Cu^{II}(Cu^{I}In^{III})_{0.5}Cl_8$ S = BA, PCA, PEA	RP ($n = 1$)	[99]

(*Continued*)

Table 1. (Continued)

Nos.	Organic spacer	LDP composition	Phase [*n*]	Refs.
49	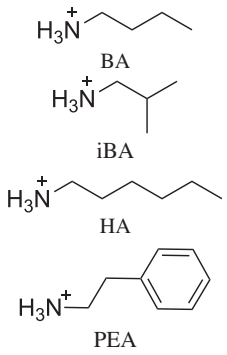 BA, iBA, HA, PEA	$(S)_4AgBiBr_8$ S = BA, iBA, HA, PEA	RP ($n = 1$)	[57]

[a] AAP = 4-aminopiperidinium; AE2T = 5,5′-diylbis(aminoethyl)-[2,2′-bithiophene]; 3AMPY = 3-(aminomethyl)pyridinium; 4AMP = 4-(ammoniummethyl)piperidinium; BA = *n*-butylammonium; BDA = 1,4-butanediammonium; BNA = benzylammonium; 3-BPA = 3-bromopropylammonium; 2ClBNA = 2-chlorobenzylammonium; 3Cl2FBNA = 3-chloro-2-fluorobenzylammonium; 1,3-CHDA = 1,3-diammoniumcyclohexane; 1,4-CHDA = 1,4-cyclohexyldiammonium; 1,4-CDMA = 1,4-bis(methylammonium)cyclohexane; CHA = cyclohexylammonium; CHpA = cycloheptylammonium; COA = cyclooctylammonium; CPA = cyclopentylammonium; 3-CPA = 3-chloropropylammonium; DA = decylammonium; DFCHA = 4,4-difluorocyclohexylammonium; DFPIP = 4,4-difluoropiperidinium; DoA = dodecylammonium; EDA = ethylenediammonium; FPEA = 4-fluorophenethylammonium; HA = hexylammonium; HIS = histammonium; MPA = 1-methylpiperidinium-4-ammonium; EPZ = 1-ethylpiperazinium; HDA = 1,6-hexanediammonium; HpDA = heptane-1,7-diammonium; iBA = isobutylammonium; 4-IBA = 4-iodobutylammonium; iPA = isopropylammonium; 3-IPA = 3-iodopropylammonium; R/S-MPA = R/S-(+/−)-*β*-methylphenethylammonium; NOE = naphthalene-*O*-ethylammonium; NOP = naphthalene-*O*-propylammonium; nPA = neopentylammonium; ODA = octane-1,8-diammonium; OA = *n*-octylammonium; PA = n-propylammonium; PCA = *p*-chloroanilinium; 1,3-PDA = 1,3-propanediammonium; PEA = 2-phenylethylammonium; POE = pyrene-*O*-ethylammonium; POP = pyrene-*O*-propylammonium; PPDA = *p*-phenylenediamine.

Phase transitions were also observed in the corresponding DJ analogue based on propane-1,3-diammonium (PDA) cations within $(PDA)_2AgRuCl_8$ compositions, which were accompanied by conformational changes upon cooling from 300 to 220 K, as demonstrated by differential scanning colorimetry.[53] Similarly, early reports on ferroelectric multilayered double perovskites were based on PA and *n*-butylammonium (BA)[39,54–56] in $(PA)_2CsAgBiBr_7$[51] and $(BA)_2CsAgBiBr_7$[54] compositions. However, their relatively low *Tc* hampered further use.[51,54] These research efforts underscored the impact of alkyl chain length and flexibility on triggering temperature-dependent phase transitions in both mono-[29,57] and bifunctional cations,[58,59] stimulating the development of relevant molecular design strategies to regulate *Tc*. Toward this goal, the lower dielectric constant of organic layers poses another bottleneck, especially in photovoltaics, which can be addressed by adjusting alkyl chain length. Instead of enhancing organic dielectric constants, shortening the interlayer distance via alkyldiammonium cations proved to be more effective.[29,52,53,58,60–64] For instance, the influence of variable spacer alkyl chain lengths was studied by comparing ethylenediammonium (EDA), PDA, and butane-1,4-diammonium (BDA) in the formation of Ag-Bi-Br LDPs, which resulted in the shortest interlayer spacing (3.76 Å) for PDA. This yielded the highest charge carrier mobility, outperforming 3D $Cs_2AgBiBr_6$ perovskites.[61]

To simultaneously tailor the interlayer spacing while enabling conformational control for desired ferroelectric and optoelectronic characteristics, using branched and cyclic spacer cations offered a promising solution, with higher *Tc* values than linear alkyl chains. For instance, branched organic cations,[49,65] such as neopentylammonium (nPA), offered 2D $(nPA)_4AgBiBr_8$ perovskite ferroelastics, with a high *Tc* and a narrower bandgap than 0D $(nPA)_4Bi_2Br_{10}$ or 1D $(nPA)_5Pb_2Br_9$.[49] Similar to bulky aliphatic cations, cyclic aliphatic ammonium (CAA) systems offered further advantages in stabilizing LDPs by strengthening intermolecular interactions in the spacer layer. Due to their cyclic geometry, CAA moieties can pack more tightly, strengthening van der Waals interactions in rigid structures that can better support inorganic layers. Such assemblies can serve as structural templates, stabilizing the perovskite structures.[66] For example, CAAs were the first to stabilize Cu-Bi-I LDPs by using cyclohexane-1,4-diammonium (1,4-CHDA) cations.[66] The size of Cu^+ and its preference for tetrahedral coordination necessitated an additional driving force to maintain the energetically unfavorable corner-sharing $[CuI_6]$ octahedron. Other cyclic mono- and diammonium species showed that six-membered rings reliably form Cu-Bi-I LDPs, whereas five-membered rings favor low-dimensional 1D frameworks. Their orientation in films was also influenced by the molecular symmetry, as 1,4-diammonium cations favored perpendicular growth onto ITO substrates, whereas asymmetric 1,3-substituted ones induced parallel or random orientations.[67] Related bifunctional spacer derivatives, such as 1,4-bis(methylammonium)cyclohexane (1,4-CDMA), were able to stabilize other trivalent metals (e.g., In, Sb, and Bi) in LDPs, such as $(1,4\text{-CDMA})_2AgMBr_8$.[68]

To maintain the improved structural control provided by spacer cyclization, while endowing the materials with improvements in charge transport, aromatic alkylammonium cations are especially relevant. They promote π–based interactions, including π–π stacking, which improves crystal quality and charge transport.[3,24–26] Arylammonium spacers, such as benzylammonium (BNA), facilitated the formation of bilayer structures like $(BNA)_2CsAgBiBr_7$ with a record *Tc* of 483 K.[69]

The stacking pattern of these structures depended on the length of the anchoring alkyl group, where parallel stacking emerged with spacers having four or more carbon atoms and parallel displacement with three-carbon-atom chains. Similarly, 2-phenylethylammonium (PEA) has been shown to produce higher-quality crystals and enhance intrinsic photoelectric properties due to the strong π–π interactions.[70–74] Various low-dimensional systems based on BNA and PEA, such as $(PEA)_4AgBiBr_8$[74,75] and $(BNA)_2CsAgBiBr_7$,[69] have been investigated. However, achieving more parallel π–π alignment of aromatic rings in such materials, relevant for charge transport, remains a challenge.[3,24–26]

To address this, fluorination can alter the aromatic ring polarization, promoting the parallel alignment of aromatic cations in adjacent layers through π–π interactions, thereby enhancing polarity, dielectric constants, and optoelectronic properties.[76] For example, the use of 4-fluorophenethylammonium (FPEA) spacers in $(FPEA)_4AgBiBr_8$ revealed that p–π coupling, a large dielectric constant, and strong interlayer binding led to improved crystal quality and electrical properties, enabling X-ray detectors.[76] This has stimulated further efforts to rely on fluorinated alkyl and arylammonium derivatives. For instance, the strategy was exploited in cyclohexylammonium (CHA) LDPs of $(CHA)_4AgSbBr_8$ composition and their difluorinated $(DFCHA)_4AgSbBr_8$ analogues. As a result, fluorination increased *Tc*, reduced the bandgap, and induced broad emission via decreased octahedral distortion and interlayer spacing.[77] Fluorine substitution increases the rotational energy barrier and the energy required for order–disorder motions of organic spacers, subsequently raising the transition temperature. Since most of the ferroelectrics undergo phase transitions accompanied by order–disorder motions, fluorine substitution represents a general approach for enhancing *Tc*.[78] The introduction of electronegative fluorine atoms also leads to stronger orbital interactions within the inorganic octahedra, thereby reducing the bandgap.[79] The first ferroelectric LDP iodide, incorporating 4,4-difluoropiperidinium (DFPIP) cations in the $(DFPIP)_4AgBiI_8$ composition, exhibited a high *Tc* value (422 K) with a large *Ps* (10.5 μC cm^{-2}) and a promising sensitivity in X-ray detection.[80] Its antimony analogue, $(DFPIP)_4AgSbI_8$, displayed similar ferroelectricity with a high *Tc* of 414 K and a large *Ps* of 9.6 μC cm^{-2}, complemented by a unique photoferroelectric behavior, indicating potential multifunctionality.[81]

The polarity of organic spacer cations and their orientation can be further tailored by other halogen substitutions. For instance, substituting the terminal methyl group in BA cation with a chlorine atom distorts the molecular geometry, giving rise to the formation of the first room-temperature ferroelectric LDP material based on 3-chloropropylammonium (3-CPA) spacers in $(3\text{-}CPA)_4AgBiBr_8$ compositions.[82] Similarly, partial bromination of 3-CPA effectively introduced noncentrosymmetric structures in $Cl_{1.14}Br_{2.86}PA_4AgInBr_8$ with a phase transition at around 460 K. Moreover, direction-dependent ferroelectricity was observed perpendicular to the octahedral layers with a maximum *Ps* of 6.25 μC cm^{-2}.[47] The stacking pattern was also dependent on the alkyl length of the organic spacer. Organic spacers with four carbon or longer alkyl chains formed [0, 0] stacking phase, whereas organic spacers with three carbon chains gave [1/2, 0] stacking phase.[53] Similarly, 4-iodobutylammonium (4-IBA) in $(4\text{-}IBA)_4AgBiI_8$ has been used in X-ray detectors.[83] However, the sensitivity of these materials to irradiation remained significantly low compared to lead-based layered perovskites, which was attributed to the intrinsic in-plane orientation associated with weak interlayer binding forces.[76] Halogen substitution in arylammonium derivatives, such as BNA, also revealed that ortho- and meta-substituents affect octahedral distortion and tilting due to the interactions with the inorganic framework.[84] This effect of halogen substitution of BNA derivatives was examined using 2-chlorobenzylammonium (2ClBNA) and 3-chloro-2-fluorobenzylammonium (3Cl2FBNA),[84] showing that the halogen atom at the ortho position affected the interaction. In particular, the Cl substituent induced octahedral distortion, whereas the smaller F resulted in octahedral tilting.

The impact of substitution on the electronic properties is pronounced in heterocyclic systems, which were predominantly used to access various DJ LDP phases. For instance, piperidine-based spacers, including 4-(ammoniummethyl)piperidinium (4AMP) and 4-aminopiperidinium (AAP), were shown to convert indirect bandgaps to direct ones in Cu-Bi LDPs by inducing favorable geometric distortions of the inorganic frameworks.[85] In particular, replacing 1,4-CHDA with 4AMP and AAP resulted in a transition from an indirect to a direct bandgap in monolayered Cu-Bi-I perovskite materials.[85] Similarly, the use of (hetero)cyclic spacer cations in Ag-Fe[60] and Ag-Sb[86] LDPs revealed that octahedral distortion plays a role in modulating bandgaps, with the least distortion yielding the narrowest bandgap,[86] showcasing important design principles with implications for the use of these lead-free alternatives in photovoltaics.

Despite these advances, most LDPs absorb primarily in the UV region, limiting their use.[87,88] This challenge has been recently addressed through the design of extended aromatic spacers, such as naphthalene and pyrene-based alkylammonium,[89] as well as bis-thiophen-diammonium cations,[41] reducing the bandgap and facilitating charge transport. The first iodide-based LDP perovskite using a bifunctional and semiconductive organic spacer, 5,5′-diylbis(aminoethyl)-[2,2′-bithiophene] (AE2T), exhibited a direct bandgap of 2 eV.[41] The initial attempts to synthesize iodide-based Ag-Bi 2D double perovskites with traditional small organic cations such as BA resulted in 0D or 1D frameworks, which is likely due to the intrinsic tendency of Bi to form lower-dimensional nonperovskite systems, aggravated by the rarity of Ag in octahedral iodide coordination. Therefore, the stabilization of I-based LDPs with the AE2T organic spacer was attributed to edge-to-face aromatic interactions. The synthesis of iodide LDPs with a simpler organic cation, 3-bromopropylammonium (3-BPA), was later achieved, which exhibited a direct bandgap while maintaining light absorption with a bandgap of 1.87 eV.[90] This suggests that molecular engineering with short-chained alkylammonium cations offers promising optoelectronic properties, competing with aryl systems. The beneficial characteristics can be further tailored by introducing *chiral* organic derivatives, such as *S*/*R*-methylphenethylammonium (*S*/*R*-MPA),[60,91] offering another gauge for tuning their properties through chirality. Further molecular engineering promises to advance their functionalities.

In summary, the molecular design of organic spacer cations, including linear, branched, and cyclic alkylammonium, as well

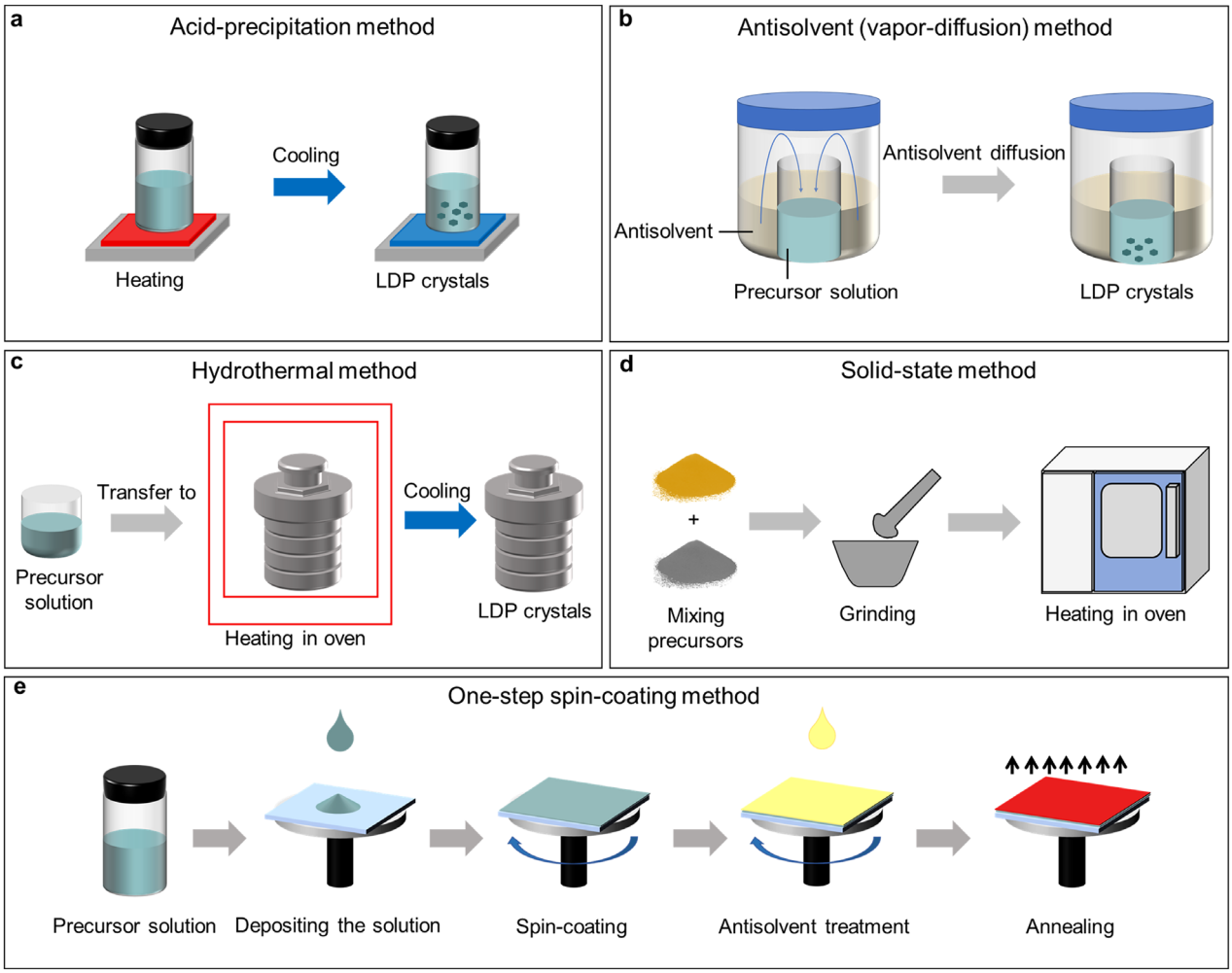

Figure 3. Schematic of synthesis methods used for LDPs to date. a) Acid-precipitation, b) antisolvent diffusion, c) hydrothermal, and d) solid-state methods, as well as e) one-step spin coating.

as arylammonium systems, has proven central to controlling structural, ferroelectric, and optoelectronic properties of LDPs. With the broad range of organic functionalities available, vast opportunities remain for rational design of multifunctional LDPs with desirable properties determining their optoelectronic characteristics and applications. To this end, appropriate synthetic methodologies are needed to realize their full potential.

3. Synthesis of LDPs

The synthesis of LDPs complement molecular engineering efforts, with the conditions influencing their crystal structure, orientation, and the resulting properties. To date, over 100 LDP different compounds with various M^+ (e.g., Ag^+, Cu^+) and M^{3+} (e.g., Bi^{3+}, Sb^{3+}, In^{3+}) compositional combinations and organic spacers (Table 1) have been reported, underscoring the versatility of molecular and material design strategies. Spacer cations determine the crystal orientations, crystallization kinetics, and interactions at organic–inorganic interfaces. A diverse range of synthetic strategies has emerged (**Figure 3a**), enabling the incorporation of structurally and electronically tailored spacers into LDP frameworks. These methods—ranging from solution processing to hydrothermal synthesis—are critical in achieving high-quality crystals and thin films for exploring structure–property relationships.

3.1. Solution-Processing Methods for LDPs

The most widely used synthesis approach for LDPs is the solution processing, which commonly leverages the solubility of metal halide or oxide precursors (e.g., AgX, BiX_3, SbX_3, InX_3, or Bi_2O_3, where X = Cl, Br, I) in hydrohalic acids (HX, X = Cl, Br, I) to access single crystals of the resulting materials (Figure 3a). The acid serves both as a solvent and a halide source for incorporation into the perovskite framework. This is followed by the addition of a precursor amine or ammonium salt of the corresponding spacer cation, while stirring at about 150 °C until a clear solution is obtained. Subsequent cooling results in the formation of perovskite crystals.[29,55] In some cases, the addition of a small amount of reducing agent, such as hypophosphorous acid (H_3PO_2), is essential for preventing the oxidation of trivalent transition metal

cations.[102] For example, Ru^{III} and Mo^{III} readily oxidize to Ru^{IV} and Mo^{IV}, respectively, in the absence of H_3PO_2, thereby hindering the synthesis of desired structures.[53] In addition, H_3PO_2 can inhibit the oxidation of Br^- to Br_3^-, effectively stabilizing the halides during the synthesis of bromide-based LDPs.[102] Perovskite crystals can thereafter be accessed either by rapid[82] or temperature-controlled cooling.[93] Different cooling rates yield crystals of varying sizes and qualities. Slow cooling typically produces larger, higher-quality crystals, while rapid cooling results in smaller crystals. Excessively large crystals may not be suitable for analysis by single-crystal X-ray diffraction (SCXRD), and the optimal crystal size can be achieved by carefully controlling the composition, solvent conditions, and cooling rate.[87]

A more versatile solution-based approach is the antisolvent (vapor diffusion) method, which is particularly useful when solution cooling fails to induce crystallization. In this case, an orthogonal "antisolvent" (i.e., solvent that cannot dissolve the target perovskite) can be added slowly to reduce the solubility and induce crystallization (Figure 3b). In a typical synthesis, precursors are dissolved in polar solvents, such as dimethyl sulfoxide (DMSO), *N,N*-dimethylformamide (DMF), or their mixture, and exposed to an antisolvent (e.g., dichloromethane, isopropanol, diethyl ether, or other) that diffuses into the solution, gradually reducing solubility and prompting crystallization (Figure 3b).[103] For example, $BA_4AgBiBr_8$ single crystals were synthesized by dissolving AgBr, $BiBr_3$, and BABr in a stoichiometric ratio of 1:1:4 in DMF:DMSO (1:7) solvent mixture and applying dichloromethane as the antisolvent in a sealed diffusion setup.[103] A simpler variation of this approach, namely antisolvent injection, triggers fast self-assembly through direct mixing of the precursor solution with the antisolvent.[74] Specifically, crystals can be accessed through a simple antisolvent recrystallization, where the precursors are dissolved in a suitable solvent to prepare the precursor solution, which is then rapidly injected into the antisolvent to trigger self-assembly.[74] Common antisolvents include isopropanol,[61] diethyl ether, chloroform,[74] and dichloromethane,[103] among others.

Alternatively, LDPs can be prepared using an acid-precipitation approach (Figure 3a), which involves mixing metal precursors with organic amine spacers in concentrated hydrohalic acid under heat treatment, followed by crystallization upon cooling.[52] For instance, $(BDA)_2AgBiBr_8$ was synthesized by mixing equimolar amounts of $BiBr_3$ and AgBr in concentrated hydrobromic acid, followed by the addition of 1,4-butanediamine, and heating at 100 °C until a clear solution was obtained. The crystals were then deposited by slowly cooling the solution (Figure 3a).[58]

Similarly, the hydrothermal method can be employed to synthesize LDPs by adding stoichiometric quantities of precursors, such as metal halides and organic amines, into aqueous HX acid and heating at 120–160 °C in a sealed autoclave (Figure 3c). The temperature and heating duration can be adjusted according to the perovskite geometry. Recently, single crystals of $(CPA)_4AgBiI_8$ were synthesized using a hydrothermal method, which involved dissolving BiI_3, AgI, and cyclopentylamine in an aqueous hydroiodic acid solution in a 1:1:4 molar ratio. The mixture was then transferred to a Teflon-lined autoclave, heated to 150 °C for 10 h, then cooled to room temperature to obtain the product crystals.[96] This approach can be relevant for accessing more challenging compositions. For instance, Sb-I-based double perovskites are relatively rare compared to their Br and Cl counterparts due to the challenging synthesis. However, 2D Cu/Sb-I-based low-dimensional double perovskites can be synthesized through the hydrothermal method by carefully selecting organic cations. For instance, a DJ phase of $(1,4\text{-CHDA})_2CuSbI_8.0.5H_2O$ composition was obtained by mixing SbI_3, CuI, and cyclohexane-1,4-diammonium in a 1:1:2 molar ratio, followed by heating in an autoclave at 160 °C for 12 h. These methods above have successfully yielded ⟨100⟩-oriented LDP structures, which were primarily characterized using SCXRD and powder X-ray diffraction (PXRD). The resulting materials were thereafter used to fabricate thin films for functional optoelectronic devices.

Another related approach for the synthesis of LDPs is the hot-injection method for lead-free perovskite nanoparticles.[107] Recently, the first synthesis of colloidal LDPs was reported using a hot-injection for perovskite nanoparticles.[108] This method involves dissolving metal salts and organic ligands in a high-boiling solvent, followed by heating the solution above 100 °C under an inert nitrogen atmosphere. Rapid injection of a cold anion precursor solution triggers nanocrystal nucleation with controlled subsequent growth. For this purpose, surfactants are often used to control the size distribution of the quantum dots.[109] For instance, colloidal $Cs_4MIn_2Cl_{12}$ (M = Cu, Co, Zn) nanocrystals were synthesized via the hot-injection method by first dissolving metal precursors (i.e., CsOAc, $Cu(OAc)_2$, $Co(OAc)_2$, or $Zn(OAc)_2$) and ligands (i.e., oleic acid and oleylamine) in 1-octadecene. The obtained solution is heated to 180 °C under an inert atmosphere, followed by the injection of chlorotrimethylsilane. Crystal growth is then prohibited by rapidly cooling the reaction mixture using an ice-water bath. The resulting nanocrystals exhibited enhanced photoluminescence with potential applications in white-light emitting devices[108] incorporating nanocrystals or thin films.

Finally, an alternative to solution-processing involves solid-state methods, such as mechanosynthesis, which have so far been rarely used for LDPs (Figure 3d). To date, there are few examples of metal halides and ammonium salts being ground (i.e., in an agate mortar) and transferred to a furnace where they are heated at 150 °C to obtain the resulting materials.[55] This could provide a more sustainable and scalable solvent-free alternative in the future.

3.2. Thin Film Fabrication and Orientation Control

Thin films of LDPs can be prepared either by one-step spin-coating or two-step methods. The one-step spin-coating method involves spin-coating precursor solutions onto a substrate, followed by thermal annealing[66] or using orthogonal solvent treatment to induce crystallization (Figure 3e).[85,90] Crystallization behavior and orientation preferences depend on several experimental factors, including solvent choice, surface treatment, and the use of additives. The orientation of the inorganic layers critically impacts charge transport. Vertical alignment is especially desirable for photovoltaic applications, as it enhances carrier mobility and boosts performance, also relevant to other optoelectronic devices.

Additives, such as ammonium chloride (NH_4Cl),[110] methylammonium chloride (MACl),[111,112] and ammonium thiocyanates (ASCN, A = NH_4^+[113] MA^+ or FA^+[114]) were found to influence the morphology and promote vertical grain alignment by modulating nucleation kinetics through different mechanisms.[115] Moreover, thiosemicarbazide (TSC), in combination with DMSO, synergistically improved crystallinity and grain size in 2D perovskites, such as $(BA)_2(MA)_3Pb_4I_{13}$, leading to reduced trap density and enhanced carrier transport.[116] Their practical application remains to be adapted to LDPs and their devices.

Film thickness also affects optoelectronic properties. It was suggested that thicker Ag/Bi-based iodide LDP films (up to 1 µm) exhibited narrower direct bandgaps and stronger light absorption, likely as a result of mixed phase formation. Here, the choice of solvent plays a crucial role in forming coordination complexes in the precursor state, which governs crystallization rates. The generally used solvents are DMSO, DMF, dimethylacetamide (DMAC), *N*-methyl-2-pyrrolidone (NMP), and γ-butyrolactone (GBL). Owing to their strong coordinating ability, they form intermediate complexes with metal ions that dictate the structure.[117] The differences in their properties (i.e., boiling point, polarity, basicity, and coordinating ability) result in the formation of different intermediates. DMF and DMSO are the most widely used precursor solvents due to their effective coordinating ability. These polar aprotic solvents act as Lewis bases to form a complex with metal ions in solution, which affects the crystallization kinetics, film morphology, and the stability of the resulting phases. To this end, while one-step spin-coating is convenient, it often results in poor film quality. In contrast, hot-casting techniques yield vertically aligned (perpendicular to the substrate) high-quality films with improved electronic characteristics, which are also organic spacer-dependent.[118]

The organic spacer identity is pivotal in directing the crystallographic orientation of thin films. Different amine spacers were found to induce distinct layer orientations in LDP films, underscoring the interplay between molecular design and crystal growth dynamics. However, the mechanistic understanding of orientation control in LDP thin films remains limited, pointing to the need for further investigation of these low-dimensional materials.

In summary, the choice of compositional elements and synthesis method exerts influence not only on the structural quality of LDPs but also on their optoelectronic properties. Achieving controlled orientation, optimal morphology, and phase purity is essential for maximizing performance in optoelectronic devices. However, the understanding of the mechanisms underlying preferential thin film orientations in LDPs is very limited. Further research is needed to gain insights into the mechanism controlling the crystallization and optoelectronic characteristics. The integration of synthetic strategies with molecular design principles will be instrumental in realizing the full potential of LDPs in next-generation optoelectronics.

4. Optoelectronic Properties of LDPs

The optoelectronic properties of LDPs are defined by the metal-halide octahedral framework templated by the organic spacer cations that are mostly electronically insulating (Figure 2 and Table 1), resulting in the charge carriers being confined within the inorganic framework. This determines their electronic behavior as quantum wells that stem from reduced dimensionality and quantum confinement effects,[119] relevant for a range of optoelectronic applications.[2,120]

As a result of their quantum well structure, the orbital interactions between the metal cations and halide anions predominantly determine the energy bandgap (**Figure 4a**). Valence band maximum (VBM) is defined by the hybridization of monovalent M-site cations′ d-orbitals and halide p-orbitals, while conduction band minimum (CBM) is typically the result of interactions with the s- or p-orbitals of the trivalent M′-site cation. For instance, the VBM of $Cs_2AgBiBr_6$ is mainly composed of Ag 4d and Br 4p orbitals, and the CBM is mainly composed of Bi 6p orbitals. For $Cs_2AgInCl_6$, the VBM consists of Ag 4d and Cl 3p orbitals, and the CBM consists of In 5s orbitals (Figure 4a,b).[121] The incorporation of organic spacer cations can indirectly influence the electronic structure through interactions with the inorganic framework, inducing structural distortions, which can lead to changes in the bandgap.[122] For instance, in $(BA)_4AgBiBr_8$, the VBM consists primarily of Ag 4d and Br 4p orbital interactions with no contribution from Bi s states, while the CBM consists primarily of Bi 6p and Br 4p orbitals. This alignment leads to a direct, larger, and more tunable bandgap compared to the indirect bandgap of the 3D counterpart (Figure 4a,b).[39] The bandgap tunability arises from the dimensionality, as well as the choice of halide and metal composition.[123] For instance, in LDPs with the general formula $(R'/R'')_{4/2}M^{I}M^{III}Cl_8$, where R′ = PA, R″ = BDA, M^{III} = In^{3+} or Ru^{3+}, and M^{I} = Cu^{+}, the selection of trivalent metal centers such as Ru^{3+} or In^{3+} directly influences the optical properties and the bandgap, ranging from 1.3 to 3.2 eV.[52] Moreover, the different numbers of inorganic layers (n) further affect the resulting bandgap.[124] In general, the bandgap of LDPs decreases with the increasing number of inorganic layers (n). For instance, $(PA)_4AgBiBr_8$ (n = 1) features a bandgap of 2.41 eV, while $(PA)_2CsAgBiBr_7$ (n = 2) was reported to have a bandgap of 2.32 eV. Similarly, the DJ $(BDA)_2AgBiBr_8$ (n = 1) was found to have a bandgap of 2.43 eV.[124] This overall suggests that the selection of metal cation, layer thickness, and quantum and dielectric confinement influence the bandgap and optoelectronic properties. Furthermore, the introduction of organic cations induces structural alterations that are reflected in the optoelectronic characteristics and can affect charge transport.[125,126]

Reduced dimensionality, dielectric confinement, and dielectric screening in LDPs contribute to their excitonic properties, with the exciton binding energies frequently surpassing 100 meV in these materials.[129] For instance, the excitonic characteristics of $(PEA)_4AgBiBr_8$ (n = 1) and $(PEA)_2CsAgBiBr_7$ (n = 2) LDPs revealed greater exciton binding energies due to reduced dimensionality.[74,76] While this can be beneficial in the light emission for LEDs, it may potentially impede efficient charge separation in solar cells. The excitonic effects can thereby be leveraged by relying on judicious material design strategies.

The charge transport properties of the LDPs are of broad interest in optoelectronic devices. The layered structure of these materials results in anisotropic characteristics with varying charge transport for in-plane and out-of-plane directions. The anisotropy can be exploited in thin-film devices, where the direction of

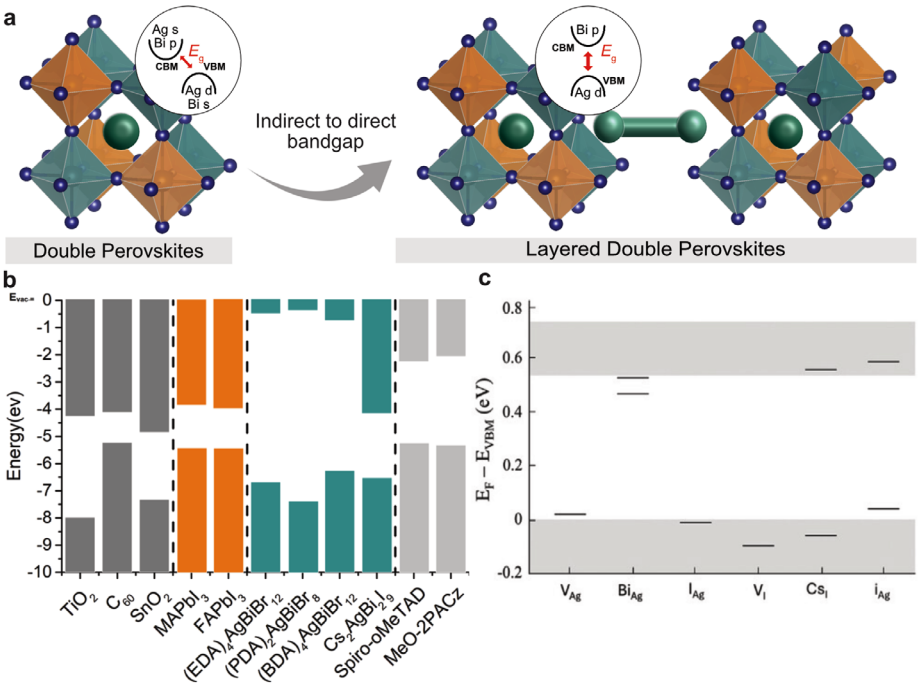

Figure 4. Optoelectronic properties of LDPs. a) Schematic of the indirect-to-direct bandgap transition from double perovskites to LDPs, with the orbital contributions in AgBiX-based LDPs. b) Comparison of band edge positions of representative lead-base 3D perovskites and LDPs compared to common electron- (ETLs) and hole-transport layers (HTLs).[127] c) Defect level positions of $Cs_2AgBi_2I_9$ compound compared to the pristine system's VBM and CBM (shown in shaded areas). Reproduced with permission.[128] Copyright 2024, John Wiley and Sons.

carrier migration influences device functionality.[130,131] For instance, 2D RP perovskites using BA and PEA spacer cations were found to exhibit efficient in-plane carrier transport, but their out-of-plane transport is highly limited due to the insulating organic layers between the inorganic sheets. With scanning photocurrent microscopy of $(BA)_2MA_{n-1}Pb_nI_{3n+1}$ 2D single crystals, in-plane carrier diffusion lengths were found to increase with the number of layers from 7 μm (n = 1) to 14 μm (n = 3), compared with 18 μm for 3D $MAPbI_3$.[131] This showcases that charge transport can be optimized through structural tailoring. In double perovskites like $Cs_2AgBiBr_6$, the ordered arrangement of alternating M-site cations (Ag^+ and Bi^{3+}) leads to a rock-salt configuration of $[AgBr_6]^{5-}$ and $[BiBr_6]^{3-}$ octahedra. Such structural ordering plays a significant role in carrier transport. The difference in electronic configuration of Ag^+ (4d) and Bi^{3+} 6p generates varied potential landscapes in the lattice and influences charge carrier delocalization. In particular, Bi^{3+} (6p) orbitals predominate in the CBM, whereas Ag 4d and Br 4p orbitals are responsible for the VBM. Such segregation causes an indirect bandgap nature and poor carrier mobility due to limited orbital overlap and high effective mass. Consequently, $Cs_2AgBiBr_6$ exhibited relatively low carrier mobility, typically 1–10 $cm^2\ V^{-1}\ s^{-1}$.[132,133] In contrast, LDPs feature more beneficial charge carrier dynamics. For instance, $(PDA)_2AgBiBr_8$ phase exhibited enhanced interlayer coupling with improved charge transport due to reduced organic spacer thicknesses and stronger hydrogen-bonding.[53,61] Moreover, an increased carrier lifetime was associated with the unique structural properties of the DJ phase, in which bifunctional PDA spacer bridges inorganic layers, enabling closer interlayer spacing and more efficient electronic coupling, reducing nonradiative recombination channels that are especially important for solar cells.[53,61] Consequently, DJ-phase LDPs tend to exhibit superior charge carrier mobility, smaller exciton binding energies, and better structural stability, favored for integration into photovoltaic and photodetector devices where efficient charge extraction capability is important.[134,135] In contrast, the van der Waals interactions between slabs in RP phases result in stronger dielectric and quantum confinement, leading to greater exciton binding energies and wider bandgaps that are better suited to light-emitting applications. Such compositional and structural tunability is reflected in the band edge alignment of the LDPs with respect to common ETLs and HTLs in devices (Figure 4c).

Most LDPs feature a wide bandgap, while some have a smaller bandgap due to structural modifications or compositional engineering.[10,28] Bandgap tunability is a key feature that enables these materials to be utilized in a wide range of optoelectronic applications.[125] LDP photoluminescence (PL) behavior also exhibits size-dependent emission,[40] attributed to quantum confinement effects and surface-related phenomena, more pronounced at the nanoscale.[52,123] It has been shown that adding transition metal ions to the LDP lattice enhances PL intensity by altering lattice rigidity and reducing nonradiative recombination channels.[136] This highlights the manner in which subtle structural changes in LDPs can directly influence emission behavior by manipulating electronic confinement and defect states. The PL response of LDPs is dominated by the stacking structure of the inorganic layers and the corresponding lattice defects.[40] It has also been shown that alterations in the adjacent octahedral layers can trigger phase transitions[94] and consequently shift the

emission spectra. Complementary studies demonstrated that the formation of self-trapped excitons in certain LDPs, induced by lattice distortion and low dimensionality, may produce enhanced or broadband luminescence,[100] which further emphasizes the significance of defect engineering.

Defect engineering enables optimizing the optoelectronic performance of LDPs. Intrinsic defects such as halide vacancies, metal interstitials, and antisite defects significantly affect carrier lifetimes, nonradiative recombination, and material stability.[137] The defect structure of LDPs with different spacers has so far not been reported, though the interstitials, antisites, and vacancies were investigated in all-inorganic $Cs_2AgBi_2I_9$ composition and it was found that all defects can form shallow traps and cannot participate in nonradiative recombination (Figure 4c). Techniques such as halide passivation, ion doping, and controlled crystallization have been attempted to suppress defect-related losses and enhance charge transport efficiency.[138] Recent work has also shown that the inclusion of passivating agents, such as organic ammonium salts or halide-mediated process conditions, can prevent deep-level trap states, leading to higher photoluminescence quantum yields (PLQY) and longer carrier lifetimes.[7–9] Furthermore, theoretical modeling and first-principles calculations have provided insight into the defect-tolerant nature of LDPs, determining that certain double perovskites possess shallow defect states, reducing deleterious charge recombination.[139] This defect tolerance, comparable to other metal-halide perovskites, enhances the potential of LDPs for stable and efficient optoelectronic applications. Further research is required, however, to establish scalable synthesis methods that maintain defect control, and ensure reproducibility and long-term material stability.[140]

To summarize, LDPs represent a highly promising platform for optoelectronics owing to their bandgap tunability, excitonic characteristics, and directional charge transport. As structure modulation and spacer chemistry affect their properties, the synergy between dimensionality, phase type, and defect states remains critical to their operation. Continuous development in defect passivation, carrier lifetime engineering, and structural optimization, with further insight into structure–property-defect interactions promises to realize the technological potential of LDPs in modern optoelectronic devices.

5. Applications of LDPs

Unique optoelectronic properties of LDPs render them suitable for a wide range of applications in optoelectronics, including solar cells, photodetectors, LEDs, photocatalysts, ferro/piezoelectrics, as well as emerging technologies, such as memristors and spintronic devices. In some cases, they are exceptionally well-suited, while in others, they offer significant advantages over alternative materials.

5.1. LDPs in Photovoltaics

The most prominent application of metal halide perovskites is in photovoltaic devices due to their direct and tunable bandgaps, high absorption coefficients, long carrier lifetimes, and high defect tolerance.[1] However, the limitations associated with their stability and Pb toxicity[141–143] stimulated efforts in developing LDPs for photovoltaics, which are still under investigation.

The first report on LDPs in solar cells was based on naphthalene- and pyrene-derivatized ammonium spacers (NOE, NOP, POE, and POP; Figure 2) in Ag-Bi or Cu-Bi LDPs.[89] These compounds showed bandgap energies of 2.2 and 2.0 eV for Ag–Bi and Cu–Bi materials, respectively, and the best performing device based on the p-i-n architectures showed short circuit current densities (J_{SC}) of 0.5 mA cm^{-2}, open circuit voltage (V_{OC}) of 0.86 V, and fill factor (FF) of 0.39, leading to the power conversion efficiencies (PCE) of 0.17%.[89] To improve these limited performances, all inorganic LDPs, such as $Cs_4CuSb_2Cl_{12}$, with a direct bandgap of 1 eV, were found very promising for solar cell applications.[144] However, photovoltaic devices based on these semiconductors have not been reported due to issues with preparing high-quality films.

In a recent study, $Cs_2AgBi_2I_9$ LDP with a bandgap of 1.78 eV, large polarons, and n-type character was synthesized and used for indoor photovoltaic application in self-powered IoT devices.[128] For this purpose, Pb toxicity and high performance under low light intensity are considered,[145] making Pb-free LDPs advantageous. It has been demonstrated that perovskite solar cells exhibit higher performance compared to c-Si solar cells under low light intensity, thereby increasing their relevance in indoor devices.[146] The $Cs_2AgBi_2I_9$ LDP devices showed 2.81% PCE under 1 Sun (**Figure 5**a,b) and 3.41% under 0.1 sun. The performance of the devices under white light LED with 1000 lux was 7.60%, with stability of T_{80} reaching 2100 min.[128] While the efficiency of more than 22% for lead-based 2D ($n = 5$)[147] and more than 6% for double perovskite[148] solar cells have been obtained so far, LDPs show great potential to achieve higher efficiencies with compositional and molecular engineering. It can be expected that by reducing the bandgap, such as via compositional engineering (e.g., replacing the Ag in common Ag-Bi compositions with large carrier effective mass and low mobility with In and Tl), increasing the n value, and relying on electroactive spacers in DJ phases, while controlling the crystallization and film growth, higher efficiencies could be obtained, especially for indoor photovoltaics.

5.2. LDPs in Photodetectors

X-ray detectors find applications in various fields, such as medical diagnosis, security inspection, and nondestructive industrial inspection. Layered halide perovskites emerged as promising materials for photodetection, particularly X-ray detectors. This anisotropic structure comprises charge-conducting channels and resistive hopping barriers oriented orthogonally. Additionally, perovskites exhibit a large attenuation coefficient, substantial carrier mobility (μ) and a long lifetime (τ) ($\mu\tau$; Figure 5c–e). They can be grown from low-cost solution processes, simplifying manufacturing.[42]

The first report on LDP for X-ray detection was in 2019, based on the $BA_2CsAgBiI_7$ system.[149] For further improving the X-ray sensitivity, a mixed-dimensional 2D/3D $(BA)_2CsAgBiBr_7/Cs_2AgBiBr_6$ X-ray detector was analyzed with sensitivity of 206 μC Gy^{-1} cm^{-2} with an ultralow dark current of 3.2×10^{-2} pA, and operational stability in a self-driven mode. This absorption characteristic for X-ray detectors is comparable

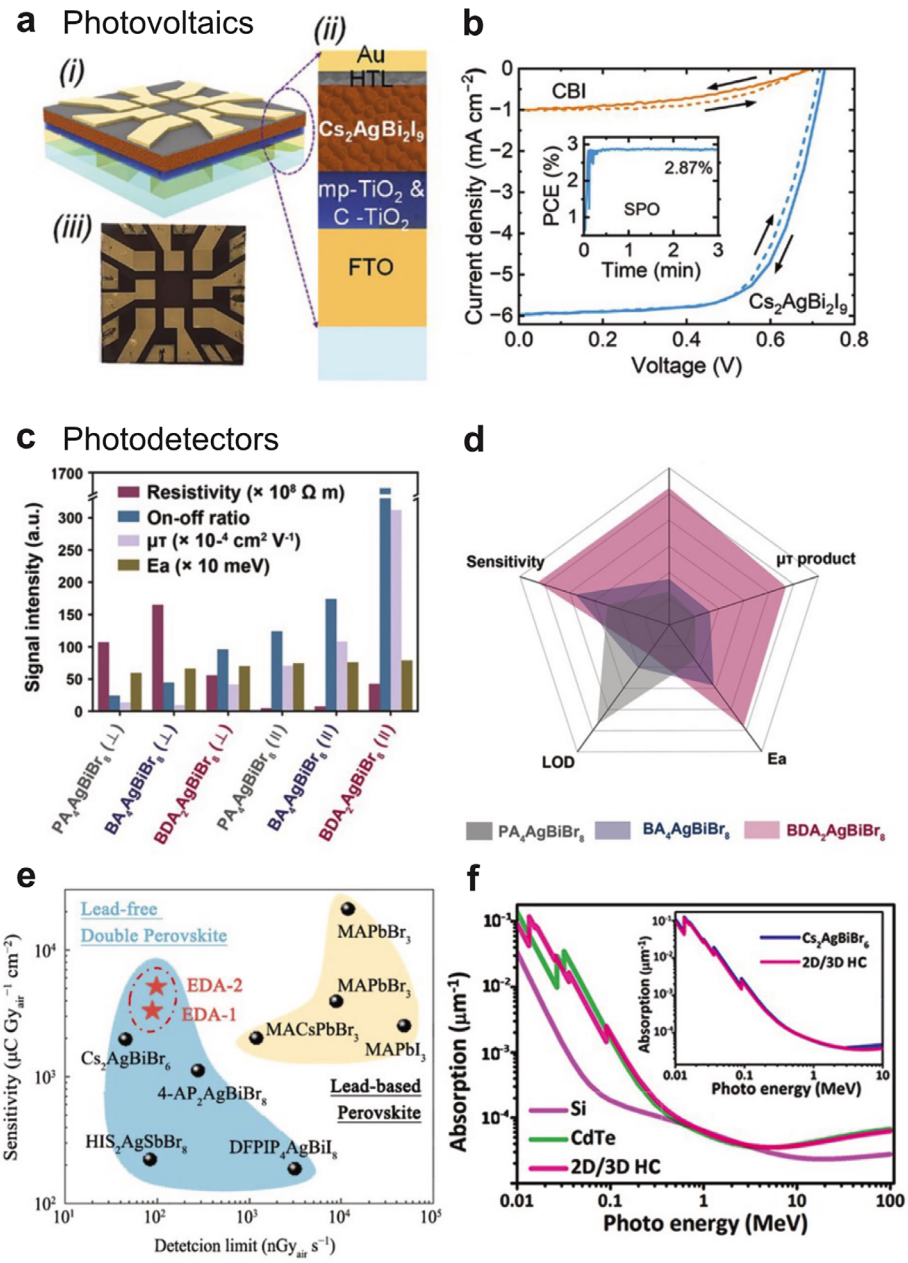

Figure 5. Application of LDPs in photovoltaics and photodetection. a) Schematic of photovoltaic device with b) *J–V* curves of the LDP and double perovskite devices. Reproduced with permission.[128] Copyright 2025, John Wiley and Sons. under CC BY 4.0. c) Comparison between parallel and horizontal charge transfer in photodetectors with d) X-ray detection performance radar maps. Reproduced with permission.[103] Copyright 2024, John Wiley and Sons. e) Comparison of sensitivity and photodetection limit of LDPs and Pb-based perovskites. Reproduced with permission.[127] Copyright 2025, John Wiley and Sons. f) Absorption of 2D/3D crystals compared to CdTe and Si. Reproduced with permission.[56] Copyright 2021, American Chemical Society.

to that of more commonly employed semiconductors, such as CdTe and Si (Figure 5f).[56] Further molecular engineering utilizing branched ammonium cations, such as nPA in $(nPA)_4AgBiBr_8$, enabled self-driven X-ray detection with high sensitivity (3.8×10^3 μC Gy^{-1} cm^{-2}) and low limit of detection (4.8 nGy s^{-1}).[150] Here, an unusual reconstruction of chemical bonds, based on the zipper-like dynamic switching of Ag–Br coordination, contributed to switchable electric polarization.[150] This conformational tailoring was further explored for CAAs, such as CPA, forming ferroelectric $(CPA)_4AgBiBr_8$ with a phase change at 343 K.[151] The layered structure with CAAs resulted in a large mobility-lifetime product of $\mu\tau = 1.0 \times 10^{-3}$ cm^2 V^{-1} for a strong response to X-ray irradiation (sensitivity value of ≈0.8 μC Gy_{air}^{-1} cm^{-2}). This value is higher than that of $MAPbI_3$ wafers (≈2×10^{-4} cm^2 V^{-1}) and $MAPbI_3$ perovskite film (≈2×10^{-7} cm^2 V^{-1}), and comparable with that of 3D $Cs_2AgBiBr_6$

crystals (≈3.75 × 10^{-3} cm^2 V^{-1}).[151] Further optimization yielded $(DFPIP)_4AgSbI_8$ LDPs with promising X-ray responsivity and a sensitivity as high as 704.8 μC Gy_{air}^{-1} cm^{-2} at 100 V bias, with a detection limit as low as 0.36 μGy_{air} s^{-1} at 10 V bias.[81] Moreover, the replacement of Sb with Bi in $(DFPIP)_4AgBiI_8$ reached the detection limits of 188 μC Gy_{air}^{-1} cm^{-2}.[80] This further illustrates the role of fluorination and the corresponding polarity enhancements in photodetection, which is particularly relevant to arylammonium cations.[76] An X-ray detector based on $(FPEA)_4AgBiBr_8$ displayed the sensitivity of the detector and detection limit of 27 μC Gy_{air}^{-1} cm^{-2} and 2.6 μGy_{air} s^{-1}, respectively,[76] with higher resistivity, higher transmittance, and much higher $\mu\tau$ compared to $(PEA)_4AgBiBr_8$.[69,74,76]

The role of molecular engineering is further exemplified in the comparison between the RP and less common DJ phases. For instance, a high sensitivity of 2638 μC Gy_{air}^{-1} cm^{-2} and an ultralow detection limit of 7.4 nGy_{air} s^{-1} was reported for DJ $(BDA)_2AgBiBr_8$, showing better performance compared to RP $(PA)_2AgBiBr_8$ and $(BA)_2AgBiBr_8$ (Figure 5c,d). These values are also much higher than those of the 3D double perovskite photodetectors based on $Cs_2AgBiBr_6$ (988 μC Gy_{air}^{-1} cm^{-2}), $Cs_2AgBiBr_6$ (1974 μC Gy_{air}^{-1} cm^{-2}), and $Cs_2AgBiCl_6$ (325.8 μC Gy_{air}^{-1} cm^{-2}).[103] The unencapsulated devices displayed tability against moisture, as well as thermal (>150 °C) and radiation (>1000 Gy_{air}) endurance with a higher attenuation coefficient compared to PA and BA-based LDPs.[103] In another study, $(EDABr)_4AgBiBr_8$ (EDA1) and $(EDABr)_4CuBiBr_8$ (EDA2) DJ phase showed sensitivities of 3388 and 5250 μC Gy_{air}^{-1} cm^{-2}, respectively. These LDPs are compared to those of other LDPs and Pb-based perovskites (Figure 5e), showing comparable sensitivity and lower limit of detection (LOD) compared to Pb-based perovskites.[127] Similarly, RP phases of $(CPA)_4AgSbI_8$, $(CHA)_4AgSbI_8$, and $(COA)_4AgSbI_8$ were compared to the DJ phases of $(1,3\text{-}CHDA)_2AgSbI_8{\cdot}H_2O$ and $(1,4\text{-}CHDA)_2AgSbI_8$ LDPs for light detection.[86] It was found that their optical bandgaps lie in the range of 2.19–2.30 eV, and the thin films exhibit preferential orientations to the substrate. The highest photocurrent of up to 17 μA cm^{-2} was achieved in $(CPA)_4AgSbI_8$ under light excitation, showcasing promising photoelectric performance for both RP and DJ LDPs.

The X-ray sensitivity of LDPs is comparable to Pb-based systems, and further molecular engineering promises to improve the X-ray attenuation coefficient while benefiting from high carrier lifetime and direct bandgap for future use in photodetection.

5.3. LDPs in LEDs

Layered perovskites can act as efficient emitters with high PLQY due to their intrinsic multiple-quantum-well characteristics, induced by reducing crystal dimensionality. Large exciton binding energy (E_b) contributes to high PLQY in layered perovskites, which is crucial for LED application.[152] The organic spacers employed in LDPs are capable of passivating crystal surface defects, thereby suppressing nonradiative recombination at grain boundaries. Furthermore, the spacers can stabilize the perovskite structure against moisture penetration and mitigate ion migration. However, the enhanced radiative recombination and stability come at the expense of color purity and carrier transfer. These drawbacks stem from the disordered phase (n) distribution and the low carrier transport capacity of large organic spacers.[152]

There have been efforts to use double perovskites for LED applications. For instance, $Cs_2AgIn_xBi_{1-x}Cl_6$ ($0 \le x \le 1$) with 2D morphology is synthesized. The corresponding nanoparticles showed the highest PLQY of 40.1%, luminance maximum of 58 cd m^{-2}, and peak current efficiency of 0.013 cd A^{-1}.[153] Furthermore, Tb^{3+} and Sb^{3+} codoped $Cs_2NaInCl_6$ nanocrystals with high PLQY blue–green emission (74%) were achieved.[154] One of the highest PLQY (90%) is achieved in $Cs_2NaInCl_6$:Sb^{3+} double perovskites made by the hydrothermal method. Similarly, LEDs based on 3% Mn^{2+}-doped $Cs_2NaTbCl_6$ enabled orange LEDs with bright PL, color rendering index (CRI) of (0.579, 0.352) and correlated color temperature (CCT) of 2547 K.[155] The only report on LDPs for LED applications was based on $Cs_4MIn_2Cl_{12}$ (M = Cu, Co, Zn) nanocrystals, showing 11.4% PLQY at ambient temperature for $Cu_4ZnInCl_{12}$ without any device demonstration.[136] The lack of use of LDPs in LEDs can be due to two main obstacles. First, the different (n) phase-mixtures in quasi-2D perovskites significantly influence the electroluminescence efficiency and stability of LEDs. Moreover, the anisotropic properties can have adverse effects on the performance, making it important to control the crystal growth.[152] By overcoming these challenges, such as through developing novel spacer cations, the introduction of additives, and adjustments in component ratios, the LDPs can be used as Pb-free LEDs with tunable color, high E_b, and low cost.

5.4. LDPs as Photocatalysts

The LDPs are a promising candidate for photocatalytic and water oxidation/CO_2 reduction applications due to their direct bandgap in the visible range, suitable band edges, relatively high absorption coefficients, and moderate carrier mobilities. Despite their potential, there are few studies on LDPs for catalytic applications. The water oxidation or CO_2 reduction by halide perovskites is thermodynamically feasible because their CBs are more negative than the H_2O and CO_2 reactions. Moreover, their bandgaps can be tuned to more than 1.23 and 1.34 eV, which are required for water splitting and CO_2 reduction, respectively.[156] However, a large overpotential is usually required to split water into O_2 and H_2 or convert CO_2 to $CO_2^{\bullet-}$, which further reacts to form formic acid, formaldehyde, CO, and methane.[156]

The photoelectrocatalysis (PEC) of LDPs is relevant to water splitting, CO_2 reduction, and pollution degradation. Based on investigation on 3D double perovskites, potential active centers consist of 1) $[M^IX_6]^{5-}$ octahedra (e.g., $[AgBr_6]^{5-}$), which can trap photoexcited electrons or holes and modify redox potentials; 2) $[M^{III}X_6]^{3-}$ octahedra (e.g., $[BiBr_6]^{3-}$, $[SbCl_6]^{3-}$), which mainly contribute to the conduction/valence band edges and play a key role in redox activity; 3) surface halide vacancies (X^-) (e.g., Br^-, I^-), which facilitate charge separation and molecular adsorption; and 4) defect sites or structural distortions, which can localize excitons and enhance photocatalytic reactions.[157–159] In water splitting, light absorption may occur by excitation in $[BiX_6]$/$[AgX_6]$ octahedra, followed by charge separation with the help of halide vacancies. The reduction site (CB edge at Ag/Bi site) and the oxidation site (VB edge, possibly at Bi/Sb site), require Bi^{3+} and

Ag^+ centers as potential redox active sites, while halide vacancies facilitate surface adsorption and charge trapping.[160] In CO_2 reduction, however, CO_2 adsorption will occur at halide vacancies or defect sites, and the photoexcitation might happen in the Bi–X or Sb–X sites. Electron transfer from CB to adsorbed CO_2 will form COOH or CHO intermediates, followed by protonation and reduction to CO, CH_4, or CH_3OH, depending on the pathway. Here, CO_2 adsorption is often facilitated by undercoordinated halide sites and M^I/M^{III}-related centers that stabilize intermediates.[156] Finally, pollution degradation consists mainly of photoexcitation to create electron-hole pairs. For hole reaction (i.e., $H_2O+h^+\rightarrow\cdot OH+H^+$) and electron reaction (i.e., $O_2+e^-\rightarrow\cdot O_2^-$), reactive radicals can form, like ·OH and $O_2^{\cdot-}$, governed by surface defects.[161] Their role in LDPs requires further mechanistic analysis.

For example, $Cs_4CuSb_2Cl_{12}$ LDP nanocrystals were used for ferricyanide reduction and Congo red dye degradation.[162] It has been demonstrated that these nanocrystals can serve as an efficient photocatalyst for ferricyanide reduction and dye degradation reactions, eliminating the need for cocatalysts.[162] In another study, these nanoparticles were utilized for a photoelectrochemical reaction due to their direct bandgap and low carrier effective mass.[163] The amperometric *I–t* curves were obtained under illumination (100 mW cm^{-2}) with a constant bias of 0.85 V versus Ag/AgCl. Rapid photoresponses were observed when the light was turned ON/OFF, and a steady-state photocurrent density of ≈6 μA cm^{-2} was achieved,[163] showcasing promise in photocatalysis.

Despite great potential, however, unlike 3D double perovskites, LDPs have not been used for photocatalytic and water oxidation/CO_2 reduction to date. It can be anticipated that these semiconductors, with a wide direct bandgap and high stability, will exhibit potential in photoelectrochemical reactions. However, their stability in harsh photoelectrochemical conditions remains a challenge, which requires further molecular engineering to stabilize the resulting materials.

5.5. LDPs in Ferroelectrics

Ferro/piezoelectric properties of LDPs arise from their noncentrosymmetric crystal structures. This allows them to accommodate dynamic polar cations between the inorganic layers in environmentally benign ferro/piezoelectrics.[164,165]

Room-temperature ferroelectricity in LDPs was first reported for 3-CPA in $(3\text{-CPA})_4AgBiBr_8$ compositions.[151] The asymmetric and polar 3-CPA enabled a phase transition from an acentric *Pc* (ferroelectric phase) state to a centrosymmetric *Pbam* (paraelectric phase) state (**Figure 6a,b**). The Curie–Weiss temperature (θ_{CW}) was 302 K for the ferroelectric phase, and the *Ps* was 3.2 μC cm^{-2} at room temperature.[151] The alternative composed of $(PA)_2CsAgBiBr_7$ exhibited a polarization of 1.5 μC cm^{-2}[54] with a low *Tc* of 220 K, which restricts its application. Alternatively, a multiaxial $(BA)_2CsAgBiBr_7$ LDP with four polarization directions demonstrated a polarization of 5.2 μC cm^{-2}, a transition temperature of ≈273 K, and an exceptionally high switching (over 10^7 cycles), comparable to that of perovskite oxides. These properties make $(BA)_2CsAgBiBr_7$ a promising candidate for energy harvesting and self-powered devices due to their lattice distortion and molecule polarizations (Figure 6c), as shown by the piezoelectric force microscopy of domain formation (Figure 6d).[166]

The corner-sharing six-coordinated octahedra constituting the inorganic scaffold in layered photoferroelectrics facilitate photoinduced charge transport. This layered structure has another advantage, namely that it provides sufficient space between layers to accommodate the dynamic motion of organic cations with a polar directional arrangement. Therefore, LDPs can be a promising "green" candidate for photoferroelectrics due to their environmental friendliness. Although these photoferroelectrics are mostly limited to Ag/Bi-based crystals, the Sb^{3+} configuration, with a similar isoelectronic structure to the Pb^{2+} ion, could also be a good candidate. LDP photoferroelectrics based on $(DFPIP)_4AgSbI_8$ showed a high *Tc* of 414 K, a large *Ps* of 9.6 μC cm^{-2}, and a relatively low bandgap of 2.2 eV.[81] $(DFPIP)_4AgSbI_8$ demonstrated a ferroelectric photovoltaic effect and photostriction (i.e., the ability to convert light energy into mechanical strain) reaching up to 1% under light radiation. The hysteresis loops at different temperatures (Figure 6b) reveal a noncentrosymmetric structure formation over 428 K.[81] The Bi-containing $(DFPIP)_4AgBiI_8$ analogue is a photoferroelectric with *Tc* of 422 K and *Ps* of 10.5 μC cm^{-2}.[80] To further increase the *Tc*, the aromatic spacer was incorporated in $(BNA)_2CsAgBiBr_7$, featuring *Ps* of 10.5 μC cm^{-2} and *Tc* of 483 K,[69] highlighting their potential in ferroelectrics.[44]

Fluorine substitution significantly enhances ferroelectric properties, particularly *Tc* and *Ps*. Moreover, fluorine substitution also improves the stability of halide perovskites by enhancing moisture and thermal resistance.[167] One of the most promising directions for further investigation is the use of the fluorinated molecules for improving different properties of LDPs, especially their stability and ferrophotovoltaic characteristics. Another underexplored research area is the development of DJ ferroelectrics. The synthesis of pure DJ phases is quite challenging and needs further investigation. Another way to widen the field of applications of ferroelectric halide perovskites is to combine it with chiral materials. Future molecular engineering efforts combined with theoretical investigations could provide a better understanding of the ferroelectric behavior and its applications in modern ferroelectrics.

5.6. LDP Memristors and Artificial Synapses

Resistive random-access memories (ReRAM) enable modern computing. The device speed, dimension, and energy efficiency with the existing flash memory technology have been identified as long-standing issues. The ReRAM operates on the basis of switchable resistance states, namely high resistance state (HRS) to low resistance state (LRS).[168] While oxides are the most extensively studied materials for ReRAM, their effectiveness is hindered by high-temperature fabrication, high power consumption, and the lack of precise control.[169]

Halide perovskites have recently gained recognition for their exceptional compatibility in ReRAMs. They are mixed ionic-electronic conductors, which is crucial for hysteresis and charge trapping, while their flexibility allows for the design of more

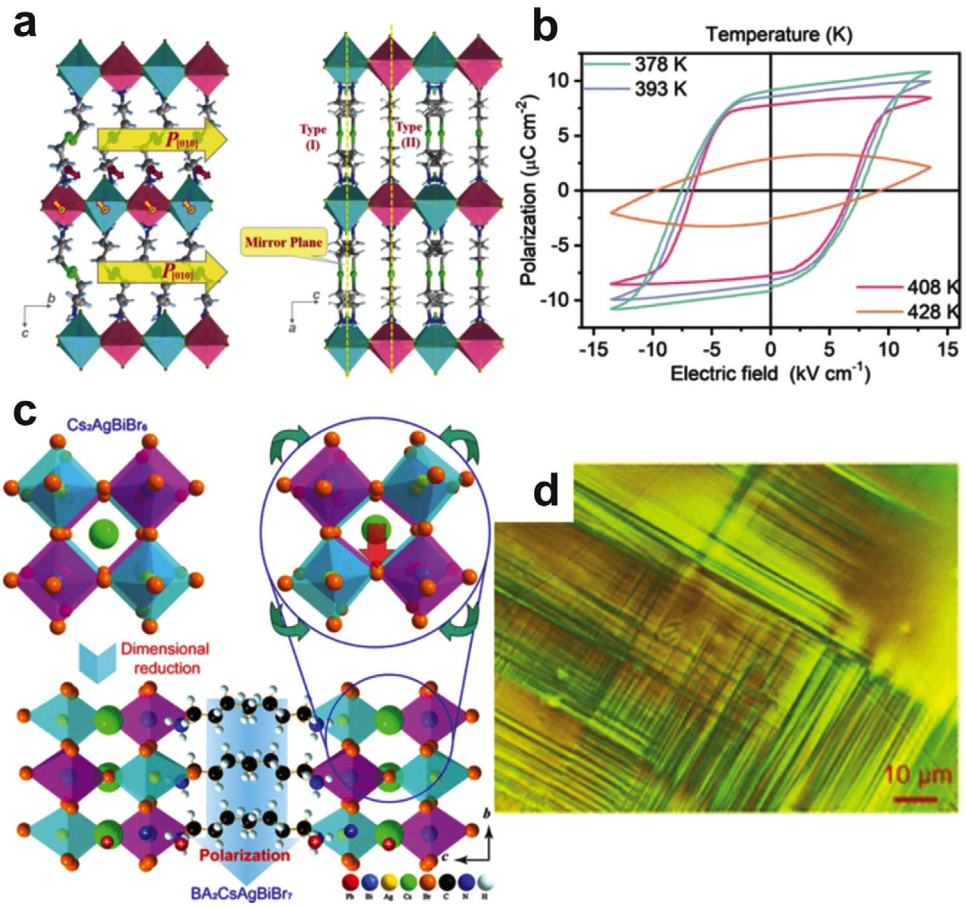

Figure 6. LDP application as ferroelectric materials. a) Polarization (left) and relaxation (right) at low and high temperature in $(3\text{-CPA})_4AgBiBr_8$. Reproduced with permission.[151] Copyright 2018, John Wiley and Sons. b) *P–E* curve of $(DFPIP)_4AgSbI_8$. Reproduced with permission.[81] Copyright 2022, John Wiley and Sons. c) Schematic of polarization induced by lattice and spacer molecule with d) polarization domain formation in $(BA)_2CsAgBiBr_7$ shown by force microscopy. Reproduced with permission.[54] Copyright 2020, American Chemical Society.

compact and efficient devices.[170] One notable example of a halide perovskite-based ReRAM is the $Cs_2AgBiBr_6$ double perovskite. This material has demonstrated remarkable stability and exceptional resistive memory properties. Notably, it exhibits superior data retention, low switching voltage, and long-term stability. However, despite these advantages, the current ON/OFF ratio is $\approx 10^2$, which is relatively poor,[171] well below the state-of-the-art of 10^6. To address this issue, dimensionality reduction has emerged as a promising solution. By dimensional reduction of the perovskite from 3D to 2D, the Schottky barrier at the electrode/perovskite interface increases. It has been reported that changing the dimensionality from 3D for $CsPbI_3$ to quasi-2D for $(PEA)_2Cs_3Pb_4I_{13}$, the bandgap widens. As the bandgap increases, the Schottky barrier height, corresponding to the electron flow from the top electrode to the bottom electrode, increases at the interface between the halide perovskite layer and Ag electrode. The increased barrier height caused a reduction of the injected carrier density from the electrode to the perovskite layer. As a result, the HRS current decreased, leading to a high ON/OFF ratio. Therefore, the dimensional reduction holds the potential to enhance the performance of ReRAMs.[172]

For this purpose, the memristor based on $(BA)_4AgBiBr_8$ was recently demonstrated and compared with 3D $Cs_2AgBiBr_6$ double perovskite.[168] Both devices showed bipolar resistive switching. The 3D double perovskite device shifts to the ON state at lower voltage compared to the LDP. Moreover, it demonstrated an ON/OFF ratio of 10^3, while the LDP device shows ON/OFF ratio of 10^6 at the compliance current (CC) of 100 μA, mainly due to the higher Schottky barrier at the interface (**Figure** 7b). In addition, the LDP device showed steady memory behavior with data retention in the order of 10^4 s and cycling endurance of 500 cycles, with the potential of multilevel programming with four different resistance states. The memory behavior of the LDP device was related to the charge trapping and the detrapping at the grain boundaries.[168] Moreover, $(BA)_2CsAgBiBr_7$ memristor demonstrated an ON/OFF ratio of up to 10^7 with a long retention time (over 2×10^4 s) and operational stability in humid conditions.[173]

The ReRAMs possess the potential in artificial synapses, effectively eliminating the distinction between computation and memory in neuromorphic computing, which mimics the human brain for artificial intelligence, sensors, robotics, and memory devices (Figure 7a).[174] This integration results in significantly enhanced energy efficiency, low power

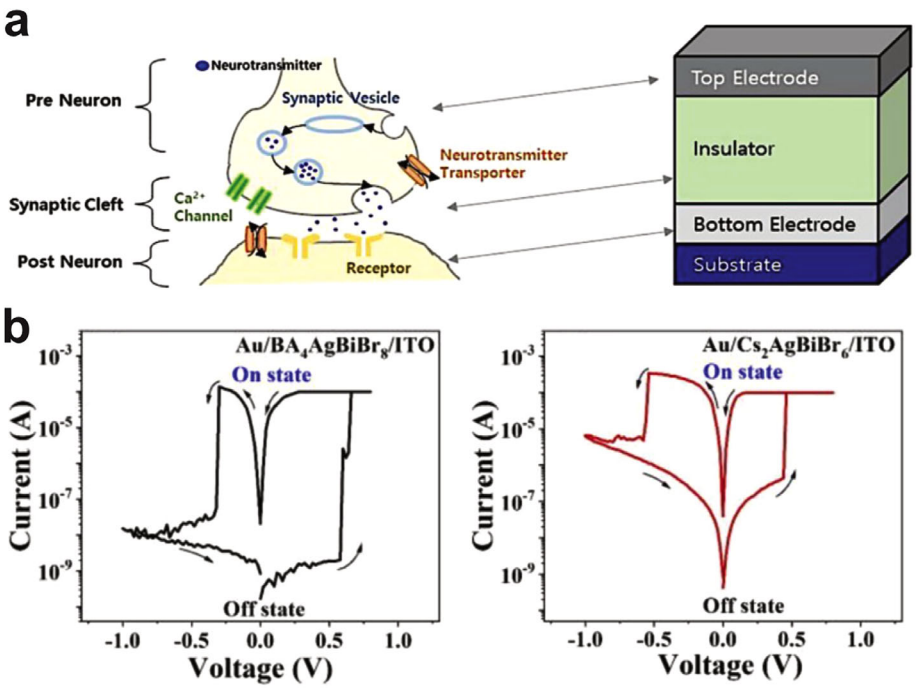

Figure 7. LPDs in memristors and artificial synapses. a) Schematic of a comparison between biological and artificial synapses. Reproduced with permission.[174] Copyright 2018, John Wiley and Sons. b) *I–V* characteristics of the $Cs_2AgBiBr_6$ DP and $(BA)_4AgBiBr_8$ LDP resistive switches for memristors and artificial synapses. Reproduced with permission.[168] Copyright 2023, American Institute of Physics.

consumption, parallel processing, and low device sizes. Perovskite memory devices still lag behind traditional memories, and optimizing their performance is a significant challenge. Substantial efforts are still needed to synthesize a high-quality perovskite active layer. The effect of defects, such as surface traps, grain boundaries, lattice strain, and vacancies, on the memristor properties remains unclear. Molecular and compositional engineering can optimize V_{set} (from HRS to LRS), V_{reset} (from LRS to HRS), ON/OFF ratio, retention time, and endurance (Figure 7b). Although the energy consumption of halide layered perovskite artificial synapses is still 4 times higher (≈400 fJ per spike) than that of biological synapses (≈100 fJ per spike), they show promising ultralow operating voltages, high ON/OFF ratio, fast response, and high endurance, as well as potential in artificial synapses, exhibiting potentiation, depression, and paired-pulse facilitation.[169] However, the LDP potential in artificial synapses has yet to be demonstrated.

5.7. LDPs in Spintronics

Magnetic halide perovskites were first reported in 1970s.[175] The development of new layered magnetic semiconductors holds immense significance for both fundamental research and practical applications, particularly in spin tronic devices. Unlike traditional inorganic 2D van der Waals crystals, such as CrI_3, $Cr_2Ge_2Te_6$, and $FePS_3$, layered metal–halide hybrid structures provide enhanced chemical and structural variation at lower temperatures.[60] This diversity allows for the easy modulation of their optical, electronic, and magnetic properties through molecular and compositional engineering. Usually, the incorporation of transition metal (Mn^{2+}, Fe^{2+}, Cr^{2+}, Cu^{2+}) and rare-earth elements (Eu^{2+}, Gd^{3+}, Sm^{3+}) with unpaired electrons (partially filled d or f orbitals) leads to magnetic halide perovskites.[176] The magnetic ordering, whether ferromagnetic or antiferromagnetic below a critical temperature, is governed by the number and arrangement of unpaired electrons. Unlike conventional magnetic materials, halide perovskites lack direct metal–metal contact. Instead, magnetic coupling occurs indirectly through halide anions and organic spacers in the perovskite lattice, in a mechanism known as superexchange interaction. This indirect exchange has a critical influence on both the strength and nature of the magnetic properties.

In double perovskites involving two different metal cations (M^+—M^{3+} or $M_1{}^{2+}$—$M_2{}^{2+}$), superexchange interactions exhibit long-range magnetic pathways due to an increased distance between the magnetic sites, resulting in weaker magnetic exchange compared to halide perovskites with a single metal cation. The superexchange interactions occur via M^{3+}—X^-—M^+—X^-—M^{3+} pathways in double perovskites consisting of a diamagnetic M^+ and a transition metal M^{3+}.[176] The dimensionality of halide perovskites also significantly affects their magnetic properties. Reduced dimensionality limits the number of nearest-neighbor magnetic interactions, potentially weakening magnetic coupling, enhancing magnetic anisotropy (i.e., increasing sensitivity to the direction of an applied field), and leading to frustrated magnetism due to competing interactions. These factors can lead to rich and complex magnetic behaviors.[177] The layered architecture of 2D perovskites gives rise to two distinct magnetic exchange interactions, namely intralayer (J) and interlayer (J') exchange. The J refers to the strong superexchange interactions that align magnetic moments within each inorganic layer.

In contrast, the J', which couples magnetic moments between adjacent layers, is generally weaker but can still have a substantial impact on the overall magnetic behavior.[176] Several structural and chemical factors can influence the nature and strength of both J and J'. First, the nature of 2D perovskite phases (i.e., RP and DJ) in terms of organic spacer configurations and octahedral connectivity across layers directly affects magnetic coupling. The DJ perovskites have a nearly linear two-halide M^{2+}–X^{-}···X–M^{2+} superexchange pathway between the layers, facilitating stronger magnetic coupling. In contrast, the RP perovskites have a nonlinear pathway with longer metal–metal distances for similar interlayer spacing. Furthermore, organic spacers form hydrogen bonds with the inorganic framework, dictating the orientation, conformation, and interlayer spacing of the structure. These interactions induce specific distortions in the inorganic octahedra, depending on whether monoammonium or diammonium cations are used. Such distortions alter metal–halide bond lengths and the X^{-}—M^{2+}—X^{-} bond angles, thereby modifying intralayer exchange. On the other hand, interlayer spacing is also a critical factor in layered perovskite systems, as the distance between adjacent layers increases, the interlayer exchange weakens, resulting in diminished magnetic coherence throughout the structure. Ultimately, the intricate magnetic behavior of 2D halide perovskites arises from the interplay between organic–inorganic interactions, structural phase, and the spacing between layers. Finally, metal-halide composition plays a critical role. The transition metal plays a dual role, introducing magnetic moments and affecting the rigidity of the inorganic framework. This, in turn, alters the hydrogen bonding network between the organic and inorganic components, influencing the overall structural and magnetic behavior. The halogen, serving as the bridge in superexchange pathways, has a direct impact on the magnetic properties. Substituting one halogen with another can significantly alter magnetic parameters, including the J and J' exchange constants. Larger halogens tend to reduce halogen–halogen distances, enhancing orbital overlap between metal ions. This typically strengthens both J and J' magnetic exchange interactions.[176]

The magnetic properties of various halide perovskites were studied and it was observed that a ferromagnetic (FM) ordering for transition metals with strong Jahn–Teller distortion (in Cu^{2+} and Cr^{2+} systems)[178] and antiferromagnetic (AFM) ordering for those without Jahn–Teller distortion (in Fe^{2+} and Mn^{2+} systems) could be achieved.[179] The mechanism behind this was explained by linear, symmetrical M—X—M linkages that result in an AFM interaction, while a superexchange pathway through different d orbitals of adjacent metal ions in Jahn—Teller-distorted $\{MX_6\}$ octahedra gives rise to a FM ordering. However, the magnetic properties of the perovskites beyond layered perovskites and new exchange mechanisms beyond M—X—M remain unknown. In double perovskites, most studies are focused on diamagnetic metal ions such as Ag^{I}—Sb^{III}, Ag^{I}—Bi^{III}, and Ag^{I}—In^{III}. However, there are few reports on the magnetic properties of transition-metal ions with unpaired electron spins.[180,181] Surprisingly, the structure and magnetic properties of Fe-based double perovskites remain largely unexplored. There are some reports on Fe-based double perovskites (e.g., $Cs_2AgFeCl_6$ and $Cs_2NaFeCl_6$), but their magnetic properties remain unknown.[182,183] When considering the LDPs, the special 2D magnetic properties with exchange mechanism beyond M-X-M still need further investigation. In this regard, $(PEA)_4AgFeCl_8$, $(R\text{-}MPA)_4AgFeCl_8$, $(BDA)_2AgFeCl_8$, and $(PEA)_4NaFeCl_8$ LDPs were studied.[60] In Fe^{3+}-containing double perovskites, the nearest Fe^{3+}—Fe^{3+} centers couple antiferromagnetically through long-range superexchange interactions following the Fe—Cl—M^{1+}—Cl—Fe pathway. The magnetic properties in these materials can be effectively tuned by altering the organic cations, bridging monovalent metal ions (M^{1+}), and dimensionality of the structure. Notably, 3D Fe—Cl double perovskites, such as $Cs_2AgFeCl_6$ and $Cs_2NaFeCl_6$, exhibit geometric magnetic frustration. However, this frustration is significantly alleviated in 2D Fe—Cl double perovskites due to the square lattice geometry, which promotes more regular magnetic ordering. A comparative analysis of monoammonium and diammonium organic spacers revealed that interlayer distances are substantially greater in RP phases (13.1–14.6 Å) than in DJ phases (3.9–4.2 Å), which enables the fine-tuning of the interlayer magnetic coupling strength, directly influencing the 2D magnetic characteristics of LDPs. DFT simulations further revealed that in-plane tilting of the perovskite framework is predominantly governed by the choice of metal ions, while out-of-plane tilting is more strongly influenced by the nature of the organic cations. Variations in bond length distortions and monovalent metal ion selection also impact the Fe–Fe distance (d_{Fe-Fe}) within the inorganic layers. For example, $(PEA)_4NaFeCl_8$ has the shortest d_{Fe-Fe} at 7.25 Å, whereas the chiral compound $(R\text{-}MPA)_4AgFeCl_8$ shows the longest at 7.73 Å. Larger structural distortion correlates with increased Fe–Fe distances, leading to weaker magnetic coupling. The larger distortion index gives rise to a longer Fe–Fe distance. This structural sensitivity allows for deliberate modulation of magnetic interactions. For $(PEA)_4AgFeCl_8$, the measured θ_{CW} is −10.7 K and the Curie constant (C) is 2.65 cm^3 K mol^{-1}, confirming AFM behavior. When varying the spacer across the Ag–FeCl series, θ_{CW} becomes progressively less negative, shifting from −10.7 K (PEA) to −3.31 K (BDA) and −1.37 K (chiral R-MPA), indicating a gradual weakening of AFM interactions. This trend is directly linked to increasing Fe–Fe distances (PEA < BDA < R-MPA) caused by structural distortion.[60] In another study, $(PEA)_4NaIn_{(1-x)}Fe_xCl_8$ LDPs. showed AFM coupling between the nearest Fe^{3+}–Fe^{3+} centers, driven by long-range superexchange interactions. The strength of this magnetic coupling can be readily tuned by adjusting the Fe^{3+} ion concentration within the lattice. The study also calculated the minimum geometrical frustration factors for these AFM-coupled alloyed systems and found that the 2D layered structures are geometrically relaxed due to their square lattice, compared to their 3D counterparts. Furthermore, they showed that key magnetic parameters are all tunable through variation in Fe^{3+} within the framework.[101] Since some of the LDPs are semiconductor magnets, they can exhibit magneto-optical properties, which can be used in optical RAM and spintronics. They can also be used for spin filtering to produce spin-polarized currents. One example is the chiral low-dimensional Cu-based system based on $(R/S\text{-}MBA)_2CuX_4$ (X = Cl, Br) (MBA = methylbenzylammonium) spin filter featuring 0D CuX_4^{2-} tetrahedral structural motifs.[184] Its spin filtering effect is attributed to chiral-induced spin selectivity (CISS), arising from the chiral structure of the material combined with a high degree of spin polarization.[184] One of the applications of

these materials has been in spin-LEDs, which are circularly polarized LEDs based on the injection of spin-polarized currents into a semiconducting emitter layer. The CISS effect has been utilized to produce spin-LEDs without the need for ferromagnetic or dilute magnetic seminconductors, enabling it to operate at room temperature without the application of magnetic field.[185–189] LDPs were recently reported in spin-LEDs based on ((*R*/*S*)-3AP)$_4$AgBiBr$_{12}$ ((*R*/*S*)-3AP = (*R*/*S*)-3-aminopyrolidone)[190] and ((*R*/*S*)-MPA)$_4$AgBiI$_8$ flat.[190,191] Moreover, chirality-induced photovoltaic effect was used to realize a self-powered X-ray detector with spontaneous electric polarization.[191]

From an application standpoint, magnetic LDPs hold significant promise in areas such as magnetic data storage, magneto-optics, sensors, spin filters, and light modulators. The ability to incorporate functional spacers in the lattice has the potential for devices with tunable magnetic properties for different applications. There is limited research on the fundamental properties of these prospective materials, and almost no research on their device integration. To bridge this gap, greater emphasis is needed on developing lab-scale prototypes and gaining a deeper understanding of key physical phenomena, such as spin-dependent photophysics and exciton polarization control. Addressing these challenges could position magnetic LDPs as leading candidates for magnetically tunable devices with advancements in spintronic and future multifunctional technologies.

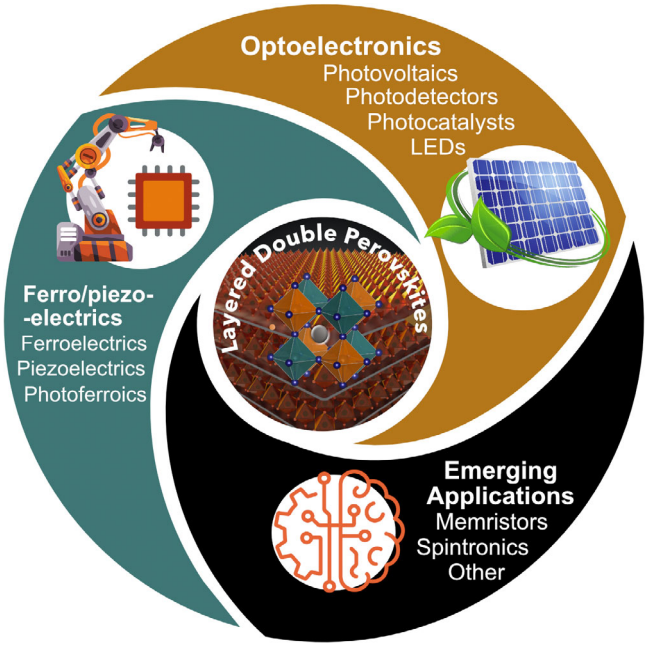

Figure 8. Schematic illustration of the prospective applications for LDPs. Image contains adapted illustrations with permission (image credit: vecstock, artnahla, and seamartini ©123rf.com).

6. Summary and Outlook

Layered double perovskites (LDPs) represent a novel and versatile class of halide perovskites that integrate key structural and electronic features from 3D organic–inorganic perovskites, quasi-2D layered perovskites, and halide double perovskites. Their structural tunability—via manipulation of A-site cations, M-site cations (M^{I} and M^{III}), halide composition, the quantum-well structure (*n*), and the organic spacer molecules, in particular—allows the formation of two main structural types, Ruddlesden–Popper (RP) and Dion–Jacobson (DJ) phases.

Molecular engineering of LDPs has advanced through a systematic evolution of spacer cation design from simple alkylammonium systems to complex semiconductive and chiral derivatives, offering unique control over structure and functionality. Early studies focused on linear alkylammonium cations, where the chain length and flexibility were shown to influence temperature-driven phase transitions and interlayer dielectric environments. To overcome the limitations of low dielectric constants in organic layers, strategies such as shortening the interlayer spacing with alkyl-diammonium cations and introducing branched or cyclic cations have been developed. Cyclic aliphatic amines provided enhanced structural stability by strengthening intermolecular van der Waals interactions, acting as rigid frameworks to stabilize otherwise unfavorable inorganic motifs. Aromatic alkylammonium cations further improved crystal quality and charge transport via π-interactions, with anchoring group length influencing stacking geometry and optoelectronic properties. Substituent modifications, particularly halogenation (e.g., fluorination), enabled control over polarity, molecular orientation, and dielectric properties, while heterocyclic systems amplified electronic tunability. To address the UV-limited absorption, semiconductive aromatic cations were introduced, extending light-harvesting capabilities. Finally, incorporating chiral organic molecules has opened new avenues for inducing noncentrosymmetric phases and ferroelectricity, adding another dimension to the design of multifunctional LDPs for optoelectronic applications.

The synthesis of LDPs commonly involves a liquid-phase route followed by spin coating to form thin films. However, achieving high-quality films remains challenging due to issues such as phase purity (including RP/DJ phase control), *n*-value heterogeneity, film uniformity, and control over crystal orientation for optimized charge transport. This limitation could be overcome in the future through an understanding of the underlying crystallization and the application of molecular design strategies to access materials with advanced properties.

Optoelectronically, LDPs exhibit a tunable transition from indirect to direct bandgaps, which are greatly influenced by composition, and are characterized by suppressed ion migration (notably in DJ phases), anisotropic charge transport, and shallow defect states. These properties make them attractive candidates for various device applications (**Figure 8**). In photovoltaics, especially for indoor light harvesting, LDPs hold promise due to their tailored bandgaps and potential operational stability, which is particularly relevant in low-light harvesting applications, such as ambient devices. However, current efficiencies lag behind state-of-the-art technologies, and long-term stability remains a critical research need. In X-ray detectors, LDPs show exceptional potential, with high sensitivity and low detection limits, which are attributes supported by their long carrier lifetimes and direct bandgaps, though the impact of organic spacers on X-ray attenuation must be managed. While the application of LEDs is still in its infancy, early results suggest high PLQYs can be driven by strong exciton binding and quantum confinement. With improved

material and device stability, LDPs could emerge as a compelling, eco-friendly option for next-generation LED technologies. Similarly, photocatalytic uses, although unexploited, particularly in water splitting and CO_2 reduction, could benefit from the inherent structural flexibility, pending validation of their stability under harsh conditions. In contrast, ferroelectricity in LDPs is a promising frontier, with reports of high *Ps* and *Tc* values tunable through spacer engineering and M-site substitutions. Innovations like fluorinated or chiral spacers, and comparisons between RP and DJ phases, present advancement opportunities.

Other emerging applications include memristors and artificial synapses, where LDPs have shown early promise in terms of device performance, which is largely unexploited. However, a deeper understanding of defect dynamics, phase influence, and other structure–property relationships is essential for further advancements. Similarly, while magnetic functionalities have been scarcely explored, early results suggest an untapped potential for spintronics in the future.

In conclusion, LDPs emerged at the intersection of rich structural chemistry and diverse application possibilities. With ongoing research to advance understanding and address current limitations in phase control, defect management, and long-term stability, molecular engineering strategies promise to enable LDPs materials in next-generation optoelectronic, spintronic, and neuromorphic technologies. We hope that this review of design principles stimulates further exploration and application.

Acknowledgements

The authors are grateful to the Editor for the invitation to contribute to the journal. M.G., M.R.G., and J.V.M. appreciate the support from the Research Council of Finland (Project No. 362642). A.M. and J.V.M. were supported by the European Research Council (ERC) under the European Union's Horizon research and innovation programme (Grant agreement No. 101114653, SmartHyMat). P.K. appreciates the European Union Scholarship for her research exchange.

Conflict of Interest

The authors declare no conflict of interest.

Keywords

halide double perovskites, layered double perovskites, molecular engineering

Received: May 16, 2025
Revised: June 30, 2025
Published online:

[1] A.-K. Jena, A. Kulkarni, T. Miyasaka, *Chem. Rev.* **2019**, *119*, 3036.
[2] L. Chouhan, S. Ghimire, C. Subrahmanyam, T. Miyasaka, V. Biju, *Chem. Soc. Rev.* **2020**, *49*, 2869.
[3] J. V. Milić, *Chimia* **2022**, *76*, 784.
[4] J.-P. Correa-Baena, M. Saliba, T. Buonassisi, M. Gratzel, A. Abate, W. Tress, A. Hagfeldt, *Science* **2017**, *358*, 739.
[5] M. Lira-Cantu, J. V. Milić, E. A. Katz, P. Troshin, T. Watson, K. Brinkmann, A. B. Djurišić, *Cell Rep. Phys. Sci.* **2022**, *3*, 101071.
[6] J. Bisquert, Y. Qi, T. Ma, Y. Yan, *ACS Energy Lett.* **2017**, *2*, 520.
[7] R. Wang, M. Mujahid, Y. Duan, Z.-K. Wang, J. Xue, Y. Yang, *Adv. Funct. Mater.* **2019**, *29*, 1808843.
[8] M. V. Khenkin, E. A. Katz, A. Abate, G. Bardizza, J. J. Berry, C. Brabec, F. Brunetti, V. Bulović, Q. Burlingame, A. Di Carlo, R. Cheacharoen, Y.-B. Cheng, A. Colsmann, S. Cros, K. Domanski, M. Dusza, C. J. Fell, S. R. Forrest, Y. Galagan, D. Di Girolamo, M. Grätzel, A. Hagfeldt, E. Hauff, H. Hoppe, J. Kettle, H. Köbler, M. S. Leite, S. F. Liu, Y.-L. Loo, J. M. Luther, et al., *Nat. Energy* **2020**, *5*, 35.
[9] H. Zhu, S. Teale, M. N. Lintangpradipto, S. Mahesh, B. Chen, M. D. McGehee, E. H. Sargent, O. M. Bakr, *Nat. Rev. Mater.* **2023**, *8*, 569.
[10] F. Giustino, H. J. Snaith, *ACS Energy Lett.* **2016**, *1*, 1233.
[11] H. Fu, *Sol. Energy Mater. Sol. Cel.* **2019**, *193*, 107.
[12] W. Ke, M. G. Kanatzidis, *Nat. Commun.* **2019**, *10*, 965.
[13] F. Cao, L. Li, *Adv. Funct. Mater.* **2020**, *4*, 2008275.
[14] T. Miyasaka, A. Kulkarni, G. M. Kim, S. Öz, A. K. Jena, *Adv. Energy Mater.* **2020**, *10*, 1902500.
[15] J. Li, H.-L. Cao, W.-B. Jiao, Q. Wang, M. Wei, I. Cantone, J. Lü, A. Abate, *Nat. Commun.* **2020**, *11*, 310.
[16] J. Li, J. Duan, X. Yang, Y. Duan, P. Yang, Q. Tang, *Nano Energy* **2021**, *80*, 105526.
[17] L. Mao, C. C. Stoumpos, M. G. Kanatzidis, *J. Am. Chem. Soc.* **2019**, *141*, 1171.
[18] B. Saparov, D. B. Mitzi, *Chem. Rev.* **2016**, *116*, 4558.
[19] G. Grancini, M. K. Nazeeruddin, *Nat. Rev. Mater.* **2019**, *4*, 4.
[20] J.-C. Blancon, J. Even, C. C. Stoumpos, M. G. Kanatzidis, A. D. Mohite, *Nat. Nanotechnol.* **2020**, *15*, 969.
[21] X. Li, J. M. Hoffman, M. G. Kanatzidis, *Chem. Rev.* **2021**, *121*, 2230.
[22] X.-G. Zhao, D. Yang, J.-C. Ren, Y. Sun, Z. Xiao, L. Zhang, *Joule* **2018**, *2*, 1662.
[23] J. V. Milic, *J. Mater. Chem. C.* **2021**, *9*, 11428.
[24] J. V. Milić, J.-H. Im, D. J. Kubicki, A. Ummadisingu, J.-Y. Seo, Y. Li, M. A. Ruiz Preciado, M. I. Dar, S. M. Zakeeruddin, L. Emsley, M. Grätzel, *Adv. Energy Mater.* **2019**, *131*, 1900284.
[25] M. Zhu, C. Li, B. Li, J. Zhang, Y. Sun, W. Guo, Z. Zhou, S. Pang, Y. Yan, *Mater. Horiz.* **2020**, *7*, 2208.
[26] W. Luo, G. AlSabeh, J. V. Milic, in *Photochemistry*, (Eds.: S. Crespi, S. Protti), Royal Society of Chemistry, Cambridge **2022**, pp. 346–370.
[27] R. Kour, S. Arya, S. Verma, J. Gupta, P. Bandhoria, V. Bharti, R. Datt, V. Gupta, *Global Challenges* **2019**, *3*, 1900050.
[28] F. Igbari, Z.-K. Wang, L.-S. Liao, *Adv. Energy Mater.* **2019**, *9*, 1803150.
[29] L. Mao, S. M. L. Teicher, C. C. Stoumpos, R. M. Kennard, R. A. DeCrescent, G. Wu, J. A. Schuller, M. L. Chabinyc, A. K. Cheetham, R. Seshadri, *J. Am. Chem. Soc.* **2019**, *141*, 19099.
[30] A. H. Slavney, T. Hu, A. M. Lindenberg, H. I. Karunadasa, *J. Am. Chem. Soc.* **2016**, *138*, 2138.
[31] E. T. McClure, M. R. Ball, W. Windl, P. M. Woodward, *Chem. Mater.* **2016**, *28*, 1348.
[32] E. Greul, M. L. Petrus, A. Binek, P. Docampo, T. Bein, *J. Mater. Chem. A* **2017**, *5*, 19972.
[33] Y. Fan, J. Fang, X. Chang, M.-C. Tang, D. Barrit, Z. Xu, Z. Jiang, J. Wen, H. Zhao, T. Niu, D.-M. Smilgies, S. Jin, Z. Liu, E. Q. Li, A. Amassian, S. (Frank) Liu, K. Zhao, *Joule* **2019**, *3*, 2485.
[34] L. Schade, S. Mahesh, G. Volonakis, M. Zacharias, B. Wenger, F. Schmidt, S. V. Kesava, D. Prabhakaran, M. Abdi-Jalebi, M. Lenz, F. Giustino, G. Longo, P. G. Radaelli, H. J. Snaith, *ACS Energy Lett.* **2021**, *6*, 1073.
[35] F. Igbari, R. Wang, Z.-K. Wang, X.-J. Ma, Q. Wang, K.-L. Wang, Y. Zhang, L.-S. Liao, Y. Yang, *Nano Lett.* **2019**, *19*, 2066.
[36] F. Ji, G. Boschloo, F. Wang, F. Gao, *Sol. RRL* **2023**, *7*, 2201112.
[37] A. Bibi, I. Lee, Y. Nah, O. Allam, H. Kim, L. N. Quan, J. Tang, A. Walsh, S. S. Jang, E. H. Sargent, D. H. Kim, *Mater. Today* **2021**, *49*, 123.

[38] W. Luo, S. Kim, N. Lempesis, L. Merten, E. Kneschaurek, M. Dankl, V. Carnevali, L. Agosta, V. Slama, Z. VanOrman, M. Siczek, W. Bury, B. Gallant, D. J. Kubicki, M. Zalibera, L. Piveteau, M. Deconinck, L. A. Guerrero-León, A. T. Frei, P. A. Gaina, E. Carteau, P. Zimmermann, A. Hinderhofer, F. Schreiber, J. Moser, Y. Vaynzof, S. Feldmann, J. Seo, U. Rothlisberger, J. V. Milić, *Adv. Sci.* **2024**, *11*, 2405622.
[39] B. A. Connor, L. Leppert, M. D. Smith, J. B. Neaton, H. I. Karunadasa, *J. Am. Chem. Soc.* **2018**, *140*, 5235.
[40] M. D. Smith, B. A. Connor, H. I. Karunadasa, *Chem. Rev.* **2019**, *119*, 3104.
[41] M. K. Jana, S. M. Janke, D. J. Dirkes, S. Dovletgeldi, C. Liu, X. Qin, K. Gundogdu, W. You, V. Blum, D. B. Mitzi, *J. Am. Chem. Soc.* **2019**, *141*, 7955.
[42] B. Vargas, G. Rodrıǵuez-López, D. Solis-Ibarra, *ACS Energy Lett.* **2020**, *5*, 3591.
[43] N. Mercier, *Angew. Chem., Int. Ed.* **2019**, *58*, 17912.
[44] M. Manzi, G. Pica, M. De Bastiani, S. Kundu, G. Grancini, M. I. Saidaminov, *J. Phys. Chem. Lett.* **2023**, *14*, 3535.
[45] W. Zhang, R. Xiong, *Chem. Rev.* **2012**, *112*, 1163.
[46] P. Siwach, P. Sikarwar, J. S. Halpati, A. K. Chandiran, *J. Mater. Chem. A* **2022**, *10*, 8719.
[47] P. Siwach, P. Sikarwar, S. A. Rajput, S. Antharjanam, A. K. Chandiran, *Chem. Commun.* **2022**, *58*, 10504.
[48] S. A. Rajput, S. Antharjanam, A. K. Chandiran, *Small* **2024**, *20*, 2403239.
[49] C. Y. Su, Y. F. Yao, Z. X. Zhang, Y. Wang, M. Chen, P. Z. Huang, Y. Zhang, W. C. Qiao, D. W. Fu, *Chem. Sci.* **2022**, *13*, 4794.
[50] J. F. Hong, B. Wang, X. Y. Zhang, H. Xu, H. X. Zhao, L. S. Long, L. S. Zheng, *Inorg. Chem.* **2022**, *61*, 20531.
[51] W. Zhang, M. Hong, J. Luo, *Angew. Chem., Int. Ed.* **2020**, *59*, 9305.
[52] A. Mandal, S. Goswami, S. Das, D. Swain, K. Biswas, *Angew. Chem., Int. Ed.* **2024**, *63*, 202406616.
[53] P. Vishnoi, J. L. Zuo, X. Li, D. C. Binwal, K. E. Wyckoff, L. Mao, L. Kautzsch, G. Wu, S. D. Wilson, M. G. Kanatzidis, R. Seshadri, A. K. Cheetham, *J. Am. Chem. Soc.* **2022**, *144*, 6661.
[54] X. Liu, Z. Xu, P. Long, Y. Yao, C. Ji, L. Li, Z. Sun, M. Hong, J. Luo, *Chem. Mater.* **2020**, *32*, 8965.
[55] E. T. McClure, A. P. McCormick, P. M. Woodward, *Inorg. Chem.* **2020**, *59*, 6010.
[56] X. Zhang, T. Zhu, C. Ji, Y. Yao, J. Luo, *J. Am. Chem. Soc.* **2021**, *143*, 20802.
[57] F. Schmitz, J. Horn, N. Dengo, A. E. Sedykh, J. Becker, E. Maiworm, P. Bélteky, Á. Kukovecz, S. Gross, F. Lamberti, K. Müller-Buschbaum, D. Schlettwein, D. Meggiolaro, M. Righetto, T. Gatti, *Chem. Mater.* **2021**, *33*, 4688.
[58] A. Mandal, S. Gupta, S. Dutta, S. K. Pati, S. Bhattacharyya, *Chem. Sci.* **2023**, *14*, 9770.
[59] L. M. Castro-Castro, A. M. Guloy, *Angew. Chem., Int. Ed.* **2003**, *42*, 2771.
[60] J. Xue, Z. Wang, A. Comstock, Z. Wang, H. H. Y. Sung, I. D. Williams, D. Sun, J. Liu, H. Lu, *Chem. Mater.* **2022**, *34*, 2813.
[61] Z. J. Bai, J. Xiong, Y. Mao, S. Tian, B. H. Wang, B. Hu, X. Wang, W. Zhou, C. T. Au, L. Chen, S. F. Yin, *Cell Rep. Phys. Sci.* **2023**, *4*, 101591.
[62] X. Xu, H. Lu, X. Zhang, L. Wang, G. Feng, L. Zheng, X. Jiang, S. Wu, S. Wang, *Angew. Chem., Int. Ed.* **2024**, 202418701.
[63] H. Chen, Z. Li, S. Wang, G. Peng, W. Lan, H. Wang, *Adv. Mater.* **2024**, *36*, 2308872.
[64] M. Chen, X. Dong, Z. Shan, Z. Xu, S. F. Liu, *J. Phys. Chem. C* **2022**, *126*, 14824.
[65] Y. Li, T. Yang, Z. Xu, X. Liu, X. Huang, S. Han, Y. Liu, M. Li, J. Luo, Z. Sun, *Angew. Chem., Int. Ed.* **2020**, *59*, 3429.
[66] L. Y. Bi, Y. Q. Hu, M. Q. Li, T. L. Hu, H. L. Zhang, X. T. Yin, W. X. Que, M. S. Lassoued, Y. Z. Zheng, *J. Mater. Chem. A* **2019**, *7*, 19662.
[67] L. Y. Bi, T. L. Hu, M. Q. Li, B. K. Ling, M. S. Lassoued, Y. Q. Hu, Z. Wu, G. Zhou, Y. Z. Zheng, *J. Mater. Chem. A* **2020**, *8*, 7288.
[68] H. Ruan, Z. Guo, J. Lin, K. Liu, L. Guo, X. Chen, J. Zhao, Q. Liu, W. Yuan, *Inorg. Chem.* **2021**, *60*, 14629.
[69] Y. Yao, H. Jiang, Y. Peng, X. Zhang, S. Chen, X. Liu, J. Luo, *J. Am. Chem. Soc.* **2021**, *143*, 15900.
[70] J. V. Milić, *J. Phys. Chem. Lett.* **2022**, *13*, 9869.
[71] M. A. Hope, T. Nakamura, P. Ahlawat, A. Mishra, M. Cordova, F. Jahanbakhshi, M. Mladenović, R. Runjhun, L. Merten, A. Hinderhofer, B. I. Carlsen, D. J. Kubicki, R. Gershoni-Poranne, T. Schneeberger, L. C. Carbone, Y. Liu, S. M. Zakeeruddin, J. Lewiński, A. Hagfeldt, F. Schreiber, U. Rothlisberger, M. Grätzel, J. V. Milić, L. Emsley, *J. Am. Chem. Soc.* **2021**, *143*, 1529.
[72] M. Almalki, A. Dučinskas, L. C. Carbone, L. Pfeifer, L. Piveteau, W. Luo, E. Lim, P. A. Gaina, P. A. Schouwink, S. M. Zakeeruddin, J. V. Milić, M. Grätzel, *Nanoscale* **2022**, *14*, 6771.
[73] M. Zhu, S. Singh, A. M. C. Chong, J.-M. Kim, F. Koc, D. P. Panda, P. Zimmermann, A. Hinderhofer, W. Luo, G. Alsabeh, M. O. UrRehman, G.-C. Choi, D. Chernyshov, F. Schreiber, J.-Y. Seo, Y. Vaynzof, A. Abate, J. V. Milic, *Adv. Sus. Energy Res.* **2025**, 2500028.
[74] X. Wang, K. Li, H. Xu, N. Ali, Y. Wang, Q. Shen, H. Wu, *Chem. Commun.* **2020**, *56*, 7917.
[75] M. E. Madjet, G. R. Berdiyorov, S. Ashhab, *Comp. Mater. Sci.* **2019**, *169*, 109130.
[76] M. Ge, S. Chen, X. Fu, Y. Feng, D. Wang, M. Yuan, *J. Phys. Chem. C* **2022**, *126*, 19417.
[77] M. Y. Wan, W. F. Liu, J. L. Luo, J. Liao, F. X. Wang, L. J. Wang, Y. Z. Tang, Y. H. Tan, *Inorg. Chem.* **2024**, *63*, 3083.
[78] Y.-Y. Tang, Y. Ai, W.-Q. Liao, P.-F. Li, Z.-X. Wang, R.-G. Xiong, *Adv. Mater.* **2019**, *31*, 1902163.
[79] B. Luo, Y. Guo, Y. Xiao, X. Lian, T. Tan, D. Liang, X. Li, X. Huang, *J. Phys. Chem. Lett.* **2019**, *10*, 5271.
[80] C.-F. Wang, H. Li, M.-G. Li, Y. Cui, X. Song, Q.-W. Wang, J.-Y. Jiang, M.-M. Hua, Q. Xu, K. Zhao, H.-Y. Ye, Y. Zhang, *Adv. Funct. Mater.* **2021**, *31*, 2009457.
[81] C.-F. Wang, H. Li, Q. Ji, C. Ma, L. Liu, H.-Y. Ye, B. Cao, G. Yuan, H.-F. Lu, D.-W. Fu, M.-G. Ju, J. Wang, K. Zhao, Y. Zhang, *Adv. Funct. Mater.* **2022**, *32*, 2205918.
[82] W. Guo, X. Liu, S. Han, Y. Liu, Z. Xu, M. Hong, J. Luo, Z. Sun, *Angew. Chem., Int. Ed.* **2020**, *59*, 13879.
[83] Z. Xu, H. Wu, D. Li, W. Wu, L. Li, J. Luo, *J. Mater. Chem. C* **2021**, *9*, 13157.
[84] J. Schimmels, W. Mihalyi-koch, C. R. Roy, K. M. Sanders, J. C. Wright, S. Jin, *Chem. Mater.* **2024**, *36*, 10605.
[85] M. S. Lassoued, L. Y. Bi, Z. Wu, G. Zhou, Y. Z. Zheng, *J. Mater. Chem. C* **2020**, *8*, 5349.
[86] Q. W. Li, M. S. Lassoued, W. P. Chen, G. Y. Gou, Y. Z. Zheng, *ACS Appl. Mater. Interfaces* **2024**, *16*, 5769.
[87] B. A. Connor, R. I. Biega, L. Leppert, H. I. Karunadasa, *Chem. Sci.* **2020**, *11*, 7708.
[88] Y. Zhang, X. Liu, H. Sun, J. Zhang, X. Gao, C. Yang, Q. Li, H. Jiang, J. Wang, D. Xu, *Angew. Chem., Int. Ed.* **2021**, *60*, 7587.
[89] R. Hooijer, S. Wang, A. Biewald, C. Eckel, M. Righetto, M. Chen, Z. Xu, D. Blätte, D. Han, H. Ebert, L. M. Herz, R. T. Weitz, A. Hartschuh, T. Bein, *J. Am. Chem. Soc.* **2024**, *146*, 26694.
[90] Y. Yao, B. Kou, Y. Peng, Z. Wu, L. Li, S. Wang, X. Zhang, X. Liu, J. Luo, *Chem. Commun.* **2020**, *56*, 3206.
[91] D. Li, X. Liu, W. Wu, Y. Peng, S. Zhao, L. Li, M. Hong, J. Luo, *Angew. Chem.* **2021**, *133*, 8496.
[92] Y. Fang, L. Zhang, L. Wu, J. Yan, Y. Lin, K. Wang, W. L. Mao, B. Zou, *Angew. Chem., Int. Ed.* **2019**, *58*, 15249.
[93] Z. Xu, X. Liu, Y. Li, X. Liu, T. Yang, C. Ji, S. Han, Y. Xu, J. Luo, Z. Sun, *Angew. Chem.* **2019**, *131*, 15904.
[94] B. Martín-García, D. Spirito, G. Bi, S. Artyukhin, F. Bonaccorso, R. Krahne, *J. Phys. Chem. Lett.* **2021**, *12*, 280.
[95] Z. Li, Q. Chen, Z. Wang, Y. Fan, T. Zhu, C. Ji, X. Kuang, J. Luo, *J. Mater. Chem. C* **2022**, *10*, 18063.

[96] M. S. Lassoued, F. Ahmad, Y. Zheng, *Chin. Chem. Lett.* **2025**, *36*, 110477.
[97] Q. W. Li, L. Y. Bi, M. S. Lassoued, Q. C. Luo, R. Yan, X. K. Ding, G. Y. Gou, Y. Z. Zheng, *Nanoscale* **2023**, *15*, 5265.
[98] M. L. Aubrey, A. Saldivar Valdes, M. R. Filip, B. A. Connor, K. P. Lindquist, J. B. Neaton, H. I. Karunadasa, *Nature* **2021**, *597*, 355.
[99] B. A. Connor, R. W. Smaha, J. Li, A. Gold-Parker, A. J. Heyer, M. F. Toney, Y. S. Lee, H. I. Karunadasa, *Chem. Sci.* **2021**, *12*, 8689.
[100] P. Yadav, S. Khurana, R. S. Lamba, S. Singh, V. Jha, S. Kumar, S. Sapra, *Adv. Opt. Mater.* **2024**, *12*, 2302456.
[101] P. Yadav, S. Khurana, D. Gill, A. Rahman, S. Bhattacharya, S. Sapra, *Chem. Mater.* **2024**, *36*, 5456.
[102] J. T. Race, T. Liu, P. M. Woodward, *Cryst. Grow. Des.* **2024**, *24*, 1367.
[103] H. Chen, Z. Li, S. Wang, G. Peng, W. Lan, H. Wang, Z. Jin, *Adv. Mater.* **2024**, *36*, 2308872.
[104] X. Li, B. Traoré, M. Kepenekian, L. Li, C. C. Stoumpos, P. Guo, J. Even, C. Katan, M. G. Kanatzidis, *Chem. Mater.* **2021**, *33*, 6206.
[105] M. S. Lassoued, T. Wang, Q. Li, X. Liu, W. Chen, B. Jiao, Q. Yang, Z. Wu, G. Zhou, S. Ding, Z. Zhang, Y. Zheng, *Mater. Chem. Front.* **2022**, *6*, 2135.
[106] Y. Zhou, L. Huang, C. Huang, M. Wu, W. Chen, Y. Pu, J. Lai, X. Tang, *J. Luminesc.* **2025**, *277*, 120914.
[107] T. Cai, W. Shi, D. J. Gosztola, K. Kobbekaduwa, H. Yang, N. Jin, Y. Nagaoka, L. Dube, J. Schneider, S. Hwang, J. Gao, X. Ma, O. Chen, *Matter* **2021**, *4*, 2936.
[108] T. Cai, W. Shi, S. Hwang, K. Kobbekaduwa, Y. Nagaoka, H. Yang, K. Hills-Kimball, H. Zhu, J. Wang, Z. Wang, Y. Liu, D. Su, J. Gao, O. Chen, *J. Am. Chem. Soc.* **2020**, *142*, 11927.
[109] Y. Mu, Z. He, K. Wang, X. Pi, S. Zhou, *iScience* **2022**, *25*, 105371.
[110] H. Xu, Y. Jiang, T. He, S. Li, H. Wang, Y. Chen, M. Yuan, J. Chen, *Adv. Funct. Mater.* **2019**, *29*, 1807696.
[111] J. M. Hoffman, C. D. Malliakas, S. Sidhik, I. Hadar, R. McClain, A. D. Mohite, M. G. Kanatzidis, *Chem. Sci.* **2020**, *11*, 12139.
[112] H. Lai, B. Kan, T. Liu, N. Zheng, Z. Xie, T. Zhou, X. Wan, X. Zhang, Y. Liu, Y. Chen, *J. Am. Chem. Soc.* **2018**, *140*, 11639.
[113] F. Li, J. Zhang, S. Jo, M. Qin, Z. Li, T. Liu, X. Lu, Z. Zhu, A. K.-Y. Jen, *Small Methods* **2020**, *4*, 1900831.
[114] H. Kim, Y. H. Lee, T. Lyu, J. H. Yoo, T. Park, J. H. Oh, *J. Mater. Chem. A* **2018**, *6*, 18173.
[115] J. Wang, D. Lin, Y. Chen, S. Luo, L. Ke, X. Ren, S. Cui, L. Zhang, Z. Li, K. Meng, Y. Lin, L. Ding, Y. Yuan, *Sol. RRL* **2020**, *4*, 2000371.
[116] H. Zheng, D. Liu, Y. Wang, Y. Yang, H. Li, T. Zhang, H. Chen, L. Ji, Z. Chen, S. Li, *Chem. Engin. J.* **2020**, *389*, 124266.
[117] Y. Su, J. Xue, A. Liu, T. Ma, L. Gao, *Molecules* **2022**, *27*, 1828.
[118] C. C. Stoumpos, C. M. M. Soe, H. Tsai, W. Nie, J.-C. Blancon, D. H. Cao, F. Liu, B. Traoré, C. Katan, J. Even, A. D. Mohite, M. G. Kanatzidis, *Chem* **2017**, *2*, 427.
[119] C. Katan, N. Mercier, J. Even, *Chem. Rev.* **2019**, *119*, 3140.
[120] L. Chu, W. Ahmad, W. Liu, J. Yang, R. Zhang, Y. Sun, J. Yang, X. Li, *Nano-Micro Lett.* **2019**, *11*, 16.
[121] S. A. Novikov, A. D. Valueva, V. V. Klepov, *Dalton Trans.* **2024**, *53*, 12442.
[122] B. A. Connor, A. C. Su, A. H. Slavney, L. Leppert, H. I. Karunadasa, *Chem. Sci.* **2023**, *14*, 11858.
[123] V. Hazra, A. Mandal, S. Bhattacharyya, *Chem. Sci.* **2024**, *15*, 7374.
[124] H. Lei, D. Hardy, F. Gao, *Adv. Funct. Mater.* **2021**, *31*, 2105898.
[125] M. Helal Miah, M. Uddin Khandaker, M. Bulu Rahman, M. Nur-E-Alam, M. Aminul Islam, *RSC Adv.* **2024**, *14*, 15876.
[126] Y. Zou, W. Yu, L. Zhang, C. Wu, L. Xiao, L. Ding, *J. Semicond.* **2021**, *42*, 120202.
[127] X. Xu, H. Lu, X. Zhang, L. Wang, G. Feng, L. Zheng, X. Jiang, S. Wu, S. Wang, *Angew. Chem., Int. Ed.* **2025**, *64*, 202418701.
[128] M. Krishnaiah, K. Singh, S. Monga, A. Tripathi, S. Karmakar, R. Kumar, C. Tyrpenou, G. Volonakis, D. Manna, P. Mäkinen, K. V. Adarsh, S. Bhattacharya, G. K. Grandhi, K. D. M. Rao, P. Vivo, *Adv. Energy Mater.* **2025**, *15*, 2404547.
[129] I. López-Fernández, D. Valli, C.-Y. Wang, S. Samanta, T. Okamoto, Y.-T. Huang, K. Sun, Y. Liu, V. S. Chirvony, A. Patra, J. Zito, L. De Trizio, D. Gaur, H.-T. Sun, Z. Xia, X. Li, H. Zeng, I. Mora-Seró, N. Pradhan, J. P. Martínez-Pastor, P. Müller-Buschbaum, V. Biju, T. Debnath, M. Saliba, E. Debroye, R. L. Z. Hoye, I. Infante, L. Manna, L. Polavarapu, *Adv. Funct. Mater.* **2024**, *34*, 2307896.
[130] J. Cho, J. T. DuBose, P. V. Kamat, *J. Phys. Chem. Lett.* **2020**, *11*, 2570.
[131] X. Wen, B. Jia, *Chem* **2022**, *8*, 904.
[132] V. Murgulov, C. Schweinle, M. Daub, H. Hillebrecht, M. Fiederle, V. Dědič, J. Franc, *J. Mater. Sci.* **2022**, *57*, 2758.
[133] W. Pan, H. Wu, J. Luo, D. Zhenzhou, C. Ge, C. Chen, X. Jiang, W.-J. Yin, G. Niu, Z. Lujun, L. Yin, Y. Zhou, Q. Xie, X. Ke, M. Sui, J. Tang, *Nat. Photonics* **2017**, *11*, 726.
[134] R. Liu, X. Hu, M. Xu, H. Ren, H. Yu, *ChemSusChem* **2023**, *16*, 202300736.
[135] S. Yudco, L. Etgar, *Adv. Opt. Mater.* **2024**, *12*, 2302592.
[136] M. Liu, S. K. Matta, T. A. Said, J. Liu, A. Matuhina, B. Al-Anesi, H. Ali-Löytty, K. Lahtonen, S. P. Russo, P. Vivo, *Small* **2024**, *20*, 2401051.
[137] F. Wang, S. Bai, W. Tress, A. Hagfeldt, F. Gao, *npj Flex Electron* **2018**, *2*, 22.
[138] D. Cortecchia, W. Mróz, S. Neutzner, T. Borzda, G. Folpini, R. Brescia, A. Petrozza, *Chem* **2019**, *5*, 2146.
[139] F.-T. Huang, B. Gao, J.-W. Kim, X. Luo, Y. Wang, M.-W. Chu, C.-K. Chang, H.-S. Sheu, S.-W. Cheong, *npj Quant. Mater.* **2016**, *1*, 16017.
[140] G. K. Grandhi, D. Hardy, M. Krishnaiah, B. Vargas, B. Al-Anesi, M. P. Suryawanshi, D. Solis-Ibarra, F. Gao, R. L. Z. Hoye, P. Vivo, *Adv. Funct. Mater.* **2024**, *34*, 2307441.
[141] C. C. Boyd, R. Cheacharoen, T. Leijtens, M. D. McGehee, *Chem. Rev.* **2018**, *119*, 3418.
[142] G. Schileo, G. Grancini, *J. Mater. Chem. C* **2021**, *9*, 67.
[143] C.-H. Chen, S.-N. Cheng, L. Cheng, Z.-K. Wang, L.-S. Liao, *Adv. Energy Mater.* **2023**, *13*, 2204144.
[144] Y. Wang, Y. Ji, Y. Yang, Z. Chen, H. Sun, X. Wang, Z. Zou, H. Huang, *ACS Energy Lett.* **2024**, *9*, 336.
[145] N. Moody, S. Sesena, D. W. deQuilettes, B. D. Dou, R. Swartwout, J. T. Buchman, A. Johnson, U. Eze, R. Brenes, M. Johnston, C. L. Haynes, V. Bulović, M. G. Bawendi, *Joule* **2020**, *4*, 970.
[146] Q. Ma, Y. Wang, L. Liu, P. Yang, W. He, X. Zhang, J. Zheng, M. Ma, M. Wan, Y. Yang, C. Zhang, T. Mahmoudi, S. Wu, C. Liu, Y.-B. Hahn, Y. Mai, *Energy Environ. Sci.* **2024**, *17*, 1637.
[147] Y. Zhang, N.-G. Park, *ACS Energy Lett.* **2022**, *7*, 757.
[148] Z. Zhang, Q. Sun, Y. Lu, F. Lu, X. Mu, S.-H. Wei, M. Sui, *Nat. Commun.* **2022**, *13*, 3397.
[149] Z. Xu, X. Liu, Y. Li, X. Liu, T. Yang, C. Ji, S. Han, Y. Xu, J. Luo, Z. Sun, *Angew. Chem., Int. Ed.* **2019**, *58*, 15757.
[150] W. Li, Y. Ma, Y. Liu, Q. Fan, H. Xu, W. Guo, L. Tang, H. Rong, Z. Sun, J. Luo, *Angew. Chem., Int. Ed.* **2025**, *64*, 202417036.
[151] W. Guo, X. Liu, S. Han, Y. Liu, Z. Xu, M. Hong, J. Luo, Z. Sun, *Angew. Chem.* **2020**, *132*, 13983.
[152] S. C. Feng, X. M. Hu, Y. Shen, Y. Q. Li, J. X. Tang, S. T. Lee, *Adv. Funct. Mater.* **2025**, *35*, 2310220.
[153] Z. Liu, Y. Sun, T. Cai, H. Yang, J. Zhao, T. Yin, C. Hao, M. Chen, W. Shi, X. Li, L. Guan, X. Li, X. Wang, A. Tang, O. Chen, *Adv. Mater.* **2023**, *35*, 2211235.
[154] H. Li, L. Tian, Z. Shi, Y. Li, C. Li, J. Feng, H. Zhang, *J. Mater. Chem. C* **2022**, *10*, 10609.
[155] A. Noculak, V. Morad, K. M. McCall, S. Yakunin, Y. Shynkarenko, M. Wörle, M. V. Kovalenko, *Chem. Mater.* **2020**, *32*, 5118.

[156] K. Bienkowski, R. Solarska, L. Trinh, J. Widera-Kalinowska, B. Al-Anesi, M. Liu, G. K. Grandhi, P. Vivo, B. Oral, B. Yılmaz, R. Yıldırım, *ACS Catal.* **2024**, *14*, 6603.
[157] K. Ren, S. Yue, C. Li, Z. Fang, K. A. M. Gasem, J. Leszczynski, S. Qu, Z. Wang, M. Fan, *J. Mater. Chem. A* **2022**, *10*, 407.
[158] F. Temerov, Y. Baghdadi, E. Rattner, S. Eslava, *ACS Appl. Energy Mater.* **2022**, *5*, 14605.
[159] X. Zhu, Y. Lin, J. San Martin, Y. Sun, D. Zhu, Y. Yan, *Nat. Commun.* **2019**, *10*, 2843.
[160] S. S. Khamgaonkar, A. Leudjo Taka, V. Maheshwari, *Adv. Funct. Mater.* **2024**, *34*, 2405414.
[161] J. Yuan, H. Liu, S. Wang, X. Li, *Nanoscale* **2021**, *13*, 10281.
[162] A. P. P., M. Joshi, D. Verma, S. Jadhav, A. R. Choudhury, D. Jana, *ACS Appl. Nano Mater.* **2021**, *4*, 1305.
[163] X.-D. Wang, N.-H. Miao, J.-F. Liao, W.-Q. Li, Y. Xie, J. Chen, Z.-M. Sun, H.-Y. Chen, D.-B. Kuang, *Nanoscale* **2019**, *11*, 5180.
[164] F. Li, D. Lin, Z. Chen, Z. Cheng, J. Wang, C. Li, Z. Xu, Q. Huang, X. Liao, L.-Q. Chen, T. R. Shrout, S. Zhang, *Nat. Mater.* **2018**, *17*, 349.
[165] W.-Q. Liao, Y. Zhang, C.-L. Hu, J.-G. Mao, H.-Y. Ye, P.-F. Li, S. D. Huang, R.-G. Xiong, *Nat. Commun.* **2015**, *6*, 7338.
[166] W. Zhang, M. Hong, J. Luo, *Angew. Chem.* **2020**, *132*, 9391.
[167] W. Zheng, X. Wang, X. Zhang, B. Chen, H. Suo, Z. Xing, Y. Wang, H.-L. Wei, J. Chen, Y. Guo, F. Wang, *Adv. Mater.* **2023**, *35*, 2205410.
[168] U. Das, H. K. Mishra, Z. Mallick, V. Gupta, A. Dehingia, A. Roy, D. Mandal, *Appl. Phys. Lett.* **2023**, *123*, 203505.
[169] M. M. Ganaie, G. Bravetti, S. Sahu, M. Kumar, J. V. Milić, *Mater. Adv.* **2024**, *5*, 1880.
[170] Y. Wang, Z. Lv, L. Zhou, X. Chen, J. Chen, Y. Zhou, V. A. L. Roy, S.-T. Han, *J. Mater. Chem. C* **2018**, *6*, 1600.
[171] S. Ghosh, H. Shankar, P. Kar, *Mater. Adv.* **2022**, *3*, 3742.
[172] H. Kim, M.-J. Choi, J. M. Suh, J. S. Han, S. G. Kim, Q. V. Le, S. Y. Kim, H. W. Jang, *NPG Asia Mater.* **2020**, *12*, 21.
[173] S.-Y. Kim, J.-M. Yang, S.-H. Lee, N.-G. Park, *Nanoscale* **2021**, *13*, 12475.
[174] S. G. Kim, J. S. Han, H. Kim, S. Y. Kim, H. W. Jang, *Adv. Mater. Technol.* **2018**, *3*, 1800457.
[175] J. P. Steadman, R. D. Willett, *Inorg. Chim. Acta* **1970**, *4*, 367.
[176] Y. Asensio, L. Olano-Vegas, S. Mattioni, M. Gobbi, F. Casanova, L. E. Hueso, B. Martín-García, *Mater. Horiz.* **2025**, *12*, 2414.
[177] L. J. de Jongh, A. R. Miedema, *Adv. Phys.* **1974**, *50*, 947.
[178] M. Abid Derbel, M. M. Turnbull, H. Naïli, W. Rekik, *Polyhedron* **2020**, *175*, 114220.
[179] J. Han, S. Nishihara, K. Inoue, M. Kurmoo, *Inorg. Chem.* **2015**, *54*, 2866.
[180] P. Vishnoi, J. L. Zuo, T. A. Strom, G. Wu, S. D. Wilson, R. Seshadri, A. K. Cheetham, *Angew. Chem.* **2020**, *132*, 9059.
[181] T. T. Tran, C. A. Pocs, Y. Zhang, M. J. Winiarski, J. Sun, M. Lee, T. M. McQueen, *Phys. Rev. B* **2020**, *101*, 235107.
[182] P. Han, C. Luo, W. Zhou, J. Hou, C. Li, D. Zheng, K. Han, *J. Phys. Chem. C* **2021**, *125*, 11743.
[183] H. Yin, Y. Xian, Y. Zhang, W. Chen, X. Wen, N. U. Rahman, Y. Long, B. Jia, J. Fan, W. Li, *Adv. Funct. Mater.* **2020**, *30*, 2002225.
[184] Y. Lu, Q. Wang, R. He, F. Zhou, X. Yang, D. Wang, H. Cao, W. He, F. Pan, Z. Yang, C. Song, *Angew. Chem., Int. Ed.* **2021**, *60*, 23578.
[185] Y.-H. Kim, Y. Zhai, H. Lu, X. Pan, C. Xiao, E. A. Gaulding, S. P. Harvey, J. J. Berry, Z. V. Vardeny, J. M. Luther, M. C. Beard, *Science* **2021**, *371*, 1129.
[186] Y. Dong, M. P. Hautzinger, M. A. Haque, M. C. Beard, *Ann. Rev. Phys. Chem.* **2025**, *76*, 519.
[187] J. Yao, Z. Wang, Y. Huang, J. Xue, D. Zhang, J. Chen, X. Chen, S.-C. Dong, H. Lu, *J. Am. Chem. Soc.* **2024**, *146*, 14157.
[188] S. Liu, J. Zerhoch, M. W. Heindl, C. Zhang, T. Kodalle, K. Sun, A. Shcherbakov, S. Bodnar, M. Miah, M. Gholipoor, C. Jandl, A. Pöthig, J. Ballmann, I. D. Sharp, P. Müller-Buschbaum, C. M. Sutter-Fella, U. W. Paetzold, F. Deschler, *J. Am. Chem. Soc.* **2025**, *147*, 16681.
[189] B. Li, Y. Li, W. Yuan, X. Zhang, S. Tao, H. Zhan, Z. Yu, K. Wang, J. Liu, L. Wang, C. Qin, *Adv. Funct. Mater.* **2025**, *35*, 2415433.
[190] Z. Yu, S. Cao, Y. Zhao, Y. Guo, M. Dong, Y. Fu, J. Zhao, J. Yang, L. Jiang, Y. Wu, *ACS Appl. Mater. Interfaces* **2022**, *14*, 39451.
[191] J. Wu, S. You, P. Yu, Q. Guan, Z.-K. Zhu, Z. Li, C. Qu, H. Zhong, L. Li, J. Luo, *ACS Energy Lett.* **2023**, *8*, 2809.

Maryam Ghasemi has been a doctoral researcher at the Department of Chemistry of the University of Turku in Finland since January 2025. She obtained her M.Sc. degree at the Sapienza University of Rome in Italy. Her research focuses on the supramolecular engineering of layered double perovskite materials in photovoltaics and beyond.

Pelin Karsili has been a postdoctoral researcher at the Department of Chemistry, University of Turku, Finland, since February 2025. She obtained her Ph.D. in Chemistry at the Eastern Mediterranean University in North Cyprus. Her research focuses on functional organic materials for hybrid perovskites and their application in lead-free photovoltaics.

Anamika Mishra has been a postdoctoral researcher at the Department of Chemistry, University of Turku, Finland, since September 2024. With extensive experience in molecular synthesis and design, her research focuses on functional organic materials for perovskite frameworks and their application in smart materials for energy conversion technologies, such as in photovoltaics.

Mohammad Reza Golobostanfard has been a senior researcher at the Department of Chemistry of the University of Turku in Finland since January 2025. He obtained his Ph.D. from the University of Tehran in 2013 in Nanomaterials Science. He worked as a Marie Sklodowska-Curie fellow on perovskite/silicon tandems in PVLAB at the EPFL in Switzerland between 2021 and 2024. His research now focuses on hybrid lead-free perovskite materials for energy conversion in photovoltaics and memristors.

Jovana V. Milić has been associate professor at the Department of Chemistry of the University of Turku in Finland since September 2024. She obtained her Ph.D. in Chemistry from the Department of Chemistry and Applied Biosciences at ETH Zurich in Switzerland in 2017. She then worked as a Scientist in the Laboratory of Photonics and Interfaces at EPFL and as assistant professor at the Adolphe Merkle Institute of the University of Fribourg in Switzerland. Her research is centered around bioinspired stimuli-responsive (supra)molecular materials for energy conversion, with a particular focus on halide perovskite materials and their application in smart (nano)technologies.